

*Scaffold Architecture and Matrix
Strain Modulate Mesenchymal Cell and
Microvascular Growth and Development in
a Time Dependent Manner*

**Gennifer Chiou, Elysa Jui, Allison
C. Rhea, Aparna Gorthi, Solaleh Miar,
Francisca M. Acosta, Cynthia Perez,
Yasir Suhail, et al.**

**Cellular and Molecular
Bioengineering**

ISSN 1865-5025


Cel. Mol. Bioeng.
DOI 10.1007/s12195-020-00648-7



Your article is protected by copyright and all rights are held exclusively by Biomedical Engineering Society. This e-offprint is for personal use only and shall not be self-archived in electronic repositories. If you wish to self-archive your article, please use the accepted manuscript version for posting on your own website. You may further deposit the accepted manuscript version in any repository, provided it is only made publicly available 12 months after official publication or later and provided acknowledgement is given to the original source of publication and a link is inserted to the published article on Springer's website. The link must be accompanied by the following text: "The final publication is available at link.springer.com".



Scaffold Architecture and Matrix Strain Modulate Mesenchymal Cell and Microvascular Growth and Development in a Time Dependent Manner

GENNIFER CHIOU,¹ ELYSA JUI,¹ ALLISON C. RHEA,¹ APARNA GORTHY,² SOLALEH MIAR,¹ FRANCISCA M. ACOSTA,¹ CYNTHIA PEREZ,¹ YASIR SUHAIL,³ KSHITIZ,^{3,4} YIDONG CHEN,² JOO L. ONG,¹ RENA BIZIOS,¹ CHRISTOPHER RATHBONE,¹ and TEJA GUDA ¹

¹Department of Biomedical Engineering and Chemical Engineering, University of Texas at San Antonio, San Antonio, TX 78249, USA; ²Greehey Children's Cancer Research Institute, University of Texas Health at San Antonio, San Antonio, TX 78229, USA; ³Department of Biomedical Engineering, University of Connecticut Health Center, Farmington, CT 06030, USA; and ⁴Cancer Systems Biology at Yale, Yale University, West Haven, CT 06516, USA

(Received 15 February 2020; accepted 11 August 2020)

Associate Editor Shelly Peyton oversaw the review of this article.

Abstract

Background—Volumetric tissue-engineered constructs are limited in development due to the dependence on well-formed vascular networks. Scaffold pore size and the mechanical properties of the matrix dictates cell attachment, proliferation and successive tissue morphogenesis. We hypothesize scaffold pore architecture also controls stromal-vessel interactions during morphogenesis.

Methods—The interaction between mesenchymal stem cells (MSCs) seeded on hydroxyapatite scaffolds of 450, 340, and 250 μm pores and microvascular fragments (MVs) seeded within 20 mg/mL fibrin hydrogels that were cast into the cell-seeded scaffolds, was assessed *in vitro* over 21 days and compared to the fibrin hydrogels without scaffold but containing both MSCs and MVs. mRNA sequencing was performed across all groups and a computational mechanics model was developed to validate architecture effects on predicting vascularization driven by stiffer matrix behavior at scaffold surfaces compared to the pore interior.

Results—Lectin staining of decalcified scaffolds showed continued vessel growth, branching and network formation at 14 days. The fibrin gel provides no resistance to spread-out capillary networks formation, with greater vessel loops within the 450 μm pores and vessels bridging across 250 μm pores. Vessel growth in the scaffolds was observed to be stimulated by hypoxia and successive angiogenic signaling. Fibrin gels showed linear fold increase in VEGF expression and no change in BMP2. Within scaffolds, there was multiple fold increase in VEGF between days 7 and 14 and early multiple fold increases in BMP2 between days 3 and 7, relative to fibrin. There was evidence of yap/taz based

hippo signaling and mechanotransduction in the scaffold groups. The vessel growth models determined by computational modeling matched the trends observed experimentally. **Conclusion**—The differing nature of hypoxia signaling between scaffold systems and mechano-transduction sensing matrix mechanics were primarily responsible for differences in osteogenic cell and microvessel growth. The computational model implicated scaffold architecture in dictating branching morphology and strain in the hydrogel within pores in dictating vessel lengths.

Keywords—Vascularization, Stroma, Scaffold, Capillaries, Bone.

INTRODUCTION

Every year millions of bone grafting procedures are performed in order to treat patients who have suffered from injury or disease that led to massive volumetric damage to bone tissue.⁷ Substantial research has focused on designing biomaterial scaffolds that promote bone regeneration to allow the patient to heal fully without the need for donor tissue from either autologous or allogeneic sources. Currently, a major limitation in the volumetric regeneration of skeletal tissue is lack of vascularization that the newly-formed bone tissue requires.²⁶ This problem is significant, since a patent vascular supply is essential in order to carry out basic physiological transport such as delivery of nutrients to cells and removal of metabolic waste.⁶¹ Without the proper vascularization of bone, degener-

Address correspondence to Teja Guda, Department of Biomedical Engineering and Chemical Engineering, University of Texas at San Antonio, San Antonio, TX 78249, USA. Electronic mail: teja.guda@utsa.edu

ation of the newly-formed tissue may lead to loss of function and necrosis, ultimately resulting in graft failure.

Highly porous, yet mechanically tough, synthetic scaffolds have been developed using a wide range of polymeric and ceramic materials and combinations thereof in an attempt to promote regeneration of the bone tissue^{11,15,22,27} Hydroxyapatite (HA), a synthetic calcium phosphate similar to the mineral constituent of bone tissue, has been widely shown to be osteoconductive^{23–25} and encourage bone regeneration within porous architectures² or around microparticles¹⁵ *in vitro*. Interconnected porosity is desired to overcome tissue infiltration limitations, but highly porous structures have poor mechanical strength and hence poor outcomes, in terms of the functional support required. While vascularization of bone tissue engineering scaffolds is an area of significant interest^{34,62,68} material- or cell-based approaches have had limited success in concurrent regeneration of functional bone and vasculature. Feng *et al.*³ reported that ceramic scaffolds with pore sizes < 400 μm limit vascular infiltration.³ Scaffolds have often been seeded with osteogenic cells to improve bone regeneration outcomes, most commonly mesenchymal stem cells (MSCs), derived from the bone marrow, because they are capable of differentiation along an osteogenic lineage,^{4,56} but also because they exert modulatory effects on host tissue by secretion of trophic factors.⁵⁸ The presence of bone stromal cells within porous scaffolds might have a three-fold impact on vascularization: (1) increased cell numbers would result in hypoxic conditions within scaffolds, which are known to induce angiogenic signaling,^{20,46} (2) paracrine signaling may induce vessel growth and (3) potential modification of the local extracellular matrix to either locally support or impede blood vessel growth. For these reasons, to improve bone graft survival and regenerative outcomes, pre-vascularization of synthetic bone graft substitutes is currently under extensive investigation^{35,65,74,78} These studies are often limited because suitable *in vitro* and *in silico* approaches to simulate vascularized tissue development are neither sufficiently advanced nor validated to be used as stringent screening tools for the optimization of novel biomaterial scaffolds.

Recent studies have shown a possible solution to pre-vascularization in the form of adipose tissue-derived microvascular fragments (MVF) which have been shown to support the growth of angiogenic tissue in several models.^{38,59} MVFs are a heterogeneous mixture of arterioles, capillaries and venules, filtered to between 40 and 400 μm in length that benefit from including the tubular vessel structure, as well as associated stem cells resident in the microvasculature.⁵⁴ These fragments have also shown retention of regen-

erative potential when placed within synthetic scaffolds to sustain proliferation of cells and secretion of growth factors vital to tissue regeneration^{8,36,63} Fibrin based hydrogels have been previously shown to promote the rapid growth and network formation of MVFs, both *in vitro* and *in vitro*^{9,48,66,70} Additionally, large amounts of microvascular fragments can be garnered from adipose tissue of the patient. Solely harvesting from patient adipose tissue could lead to the use of minimal amount of orthotopic tissue from the patient to increase regeneration of musculoskeletal tissue while also decreasing the chance of subsequent rejection of the pre-vascularized grafts as is the case with allografts or xenografts. For this strategy, the time dependence relied on by angiogenesis (vascular ingrowth from the host) is circumvented since blood vessels or vascular networks within implants need to form connections among themselves and inosculate with the host vasculature for long term perfusion and successful engraftment to be possible.³⁷ Fibrin hydrogels also mimic the *in situ* blood clot (fracture hematoma) that forms at the bone defect site after injury, in that they include the entangled fibrin mesh, but not the inflammatory cytokines from the platelet plug *in vitro*.³² Fibrin hydrogels and composites thereof have been previously investigated to support bone regeneration in conjunction with biologic or growth factor delivery strategies.^{29,53}

Many biomaterials have been developed for use as vascularized grafts; their limited success, however, necessitates further development, which is impeded by a poor understanding of the specific design parameters which can be optimized to induce enhanced vascularization. The interplay of biochemical, biological and fluid flow variables in the development of vasculature has been extensively studied, but the impact of the mechanics of the tissue extracellular matrix (ECM) and the temporal dynamics of the resistivity (or lack thereof) of the ECM to tissue ingrowth have been largely ignored. This is especially the case for vascular development within tissue regenerative matrices where small caliber capillary networks are necessary. In order to address these challenges, the current study attempts to reconcile three distinct metrics: (1) dynamics of multi-tissue development within biomaterial scaffolds, (2) the underlying cell-signaling pathways, and (3) understanding the impact of matrix mechanics as an independent variable to predict morphological development of vascular networks. The concurrent attachment, proliferation and commitment to bone-specific phenotype of bone-marrow-derived mesenchymal stem cells (MSCs) and growth, branching and capillary morphogenesis of MVFs in fibrin hydrogel filled-porous hydroxyapatite (HA) scaffolds is evaluated *in vitro* over 3 weeks (schematic in Fig. 1). The temporal

dynamics within the multi-lineage culture system are evaluated in an attempt to understand their impact on vascularized tissue development. Furthermore, a computational mechanics model is developed to model blood vessel growth within highly porous synthetic biomaterials taking into account local matrix stiffness gradients—i.e. a fibrin or entangled protein hydrogel within the pore of a stiff, porous scaffold is softer near the center of the pore and stiffest at the scaffold surface. The overall hypothesis of this study is that the pore size of scaffolds thus impacts how vessel networks and osteoid like tissue form within biomaterial scaffolds over time.

METHODS

HA Scaffold Preparation

Calcium phosphate scaffolds were synthesized *via* a template coating method using polyurethane foams of varying pore sizes (45, 60, and 80 pores per inch), as described previously.²⁴ Briefly, a hydroxyapatite (HA) (CaP Biomaterials LLC, East Troy, WI) based slurry was prepared using 5% high molecular weight polyvinyl alcohol, 5% carboxymethyl cellulose, 3% ammonium polyacrylate dispersant, and 10% N,N-dimethylformamide (as binders to help the stabilization and sintering of the scaffold). The slurry was coated over polyurethane foams (8 mm diameter and 2 mm height), and pore sizes of 45, 60, and 80 pores per inch which, will be referred to as 450, 340 and

250 μm pore size scaffolds, respectively, based on their architectural characterization.^{23,24} Samples were allowed to dry followed by sintering in a furnace (Zircar Zirconia, Florida, NY) to a peak value of 1240 $^{\circ}\text{C}$ for 20 h. The sintered scaffolds were coated for a second time with the HA based slurry, dried overnight, and sintered again. All chemical supplies were purchased from Sigma Aldrich (St. Louis, MO) unless otherwise specified.

Scaffold Characterization

Scanning electron microscopy (SEM) evaluation was performed at 40X magnification to measure the strut thickness and strut length (25 measurements per scaffold, $n = 4$ scaffolds/pore size) and quantify pore size. All microscopy was performed on an JEOL 6610 (JEOL Ltd., Tokyo, Japan) at 20 kV. One hundred independent struts were measured across four scaffolds per architecture of interest to the present study, and averaged to determine strut length as an estimate of pore interconnection/opening size.

Porosity was determined using an AccuPyc II Helium pycnometer (Micromeritics, Norcross, GA) to determine the skeletal volume of each scaffold ($n = 6$ scaffolds per architecture). Based on measurements of the average scaffold diameter and height, the envelope volume of each scaffold was calculated. Using the ratio of skeletal volume to envelope volume, porosity was determined using the following equation:

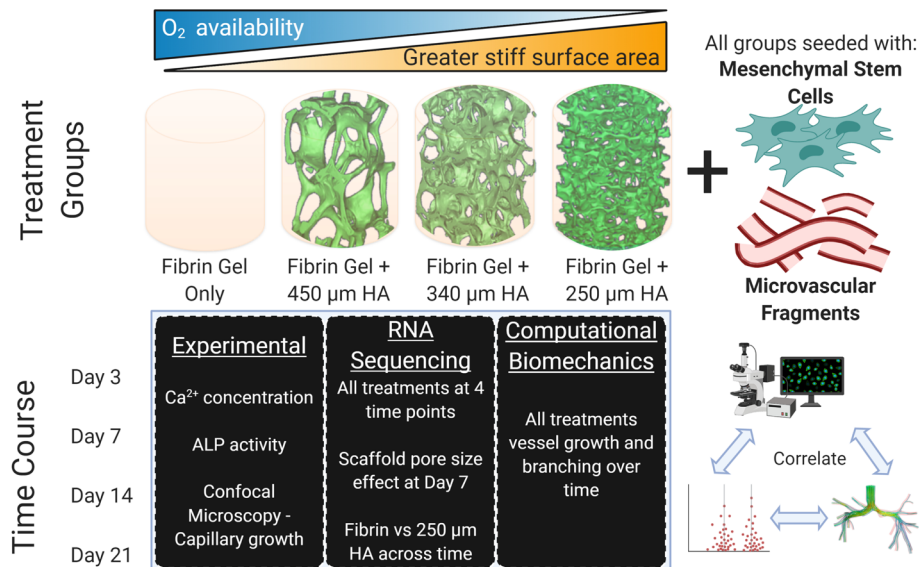


FIGURE 1. Experimental design. The experiment is based on MSCs seeded on HA scaffolds (450, 340 and 250 μm pore sizes) which are then infiltrated and filled with fibrin hydrogels containing MVFs. The control group is a fibrin hydrogel containing MVFs, with MSCs seeded at the base (mimicking an infinite pore). These scaffolds are evaluated over 21 days of *in vitro* culture (at day 3, 7, 14 and 21), with multiple experimental analyses (left box), RNA sequencing analysis and 2 sub-analyses (middle box) and compared to a computational biomechanics model (right box).

$$\text{Porosity}(\%) = \left(1 - \frac{\text{Skeletal Volume}}{\text{Envelope Volume}}\right) \times 100 \quad (1)$$

Scaffold permeability was measured using a custom flow apparatus consisting of a fluid reservoir that fed into a sample chamber opened to the atmosphere. The pressure head was thus equal to the height of the liquid column above the sample holder. Using Darcy's Law, permeability was determined as:

$$k = \left(\frac{m\mu L}{A_{cs}\rho\Delta P}\right) \quad (2)$$

where k is the permeability, m is the mass flow rate, μ is the fluid viscosity, L is the specimen length, A_{cs} is the mean cross sectional area of the specimen, ρ is the fluid density, and ΔP is the pressure drop across the scaffold. Distilled water was used for the permeability measurements. Each scaffold was equilibrated by repeatedly running water through it for 5 min prior to testing. Permeability was then computed by measuring the volume of effluent water collected over four different lengths of time through each scaffold. All measurements for porosity and permeability were performed in triplicate for 6 scaffolds per architecture of interest to the present study.

Each scaffold was scanned using micro computed tomography (μ CT), as previously reported.²⁴ Briefly, scanning was performed at 100 kV and 100 μ A source settings with no filter on a SkyScan 1076 (Bruker Skyscan, Belgium) at 8.87 μ m spatial resolution. Morphometric analysis was carried out on CT images using CTAnalyzer vs.1.4 (Skyscan) for 6 scaffolds per architecture. In order to determine trabecular bone organization, 9 traditional histomorphometric parameters were computed for each scaffold tested over its 3-D volume. The 9 parameters computed were bone volume ratio (BV/TV), bone surface to total volume ratio (BS/TV), bone surface density (BS/BV), trabecular pattern factor (Tb.Pf), structural model index (SMI), trabecular thickness (Tb.Th), trabecular number (Tb.N), trabecular spacing (Tb.Sp.), and degree of anisotropy (DA).

Rat Bone Marrow-MSc and Adipose MVF Isolation and Culture

Bone-marrow-derived mesenchymal stem cells (MSCs) were isolated from the femurs of wild type male Lewis rats (Charles River Laboratories, Wilmington, MA) using a modified version of a protocol.⁴⁰ Briefly, the rats were euthanized using CO₂ asphyxiation. The femurs were excised and remaining soft tissue was removed. The ends of each femur were scored using a scalpel and cut with a rongeur. The bone

marrow of the femur was flushed out using cell culture medium consisting of α -MEM (Gibco, Carlsbad, CA), supplemented with 15% FBS (ATCC, Manassas, VA), 1% PSA (Gibco), and Mycozap (Lonza, Houston, TX) delivered through an 18-gauge needle. The femur was flushed until the bone appeared white. The collected flushed bone-marrow media was transferred to a tissue culture T25 flask (Corning, Corning, NY) and the collected MSCs were allowed to adhere for 24 h under standard culture conditions. At that time, the supernatant media and nonadherent cells were aspirated and the adherent cells were rinsed with 37 °C PBS 3 times. Fresh cell culture media was then added and the adherent cells cultured until confluency. During this time, the supernatant medium was changed every 3–4 days with alternating full and half media changes. MSCs were used for the experiment at passage 5.

Microvascular fragments (MVF) were isolated from the inguinal, subcutaneous, and epididymal fat pads of wild type male Lewis rats (Charles River Laboratories).^{48,55} Briefly, the fat pads were minced with scissors and subjected to digestion using collagenase (Worthington Biochemical Corporation, Lakewood, NJ) at 37 °C with agitation or 8–20 min. The digested fat was filtered and washed through 500 μ m and 37 μ m filters to remove debris and prevent contamination. MVFs were collected and immediately seeded in fibrin gels either directly (control group) or within the three architectures of HA scaffolds of interest to the present study.

In Vitro Study Design and Analyses

MSCs at passage 5 were seeded onto HA scaffolds at a density of 200,000 cells/scaffold⁵⁸ and were allowed to adhere for 24 h under standard cell culture conditions. For the control group, MSCs were seeded onto tissue-culture 48 well plates and were cultured in MSC growth media. HA scaffolds preseeded with MSCs, were then infiltrated with MVFs and fibrin gels⁵⁷ at a MVF density of 20,000 MVF/mL. A total gel volume of 125 μ L was created by combining fibrinogen from bovine plasma (20 mg/mL) (Type I-S, 65–85% protein, Sigma Aldrich) and thrombin (MilliporeSigma, Burlington, MA) at a ratio of 2–5, respectively with the ~ 2500 MVFs. HA scaffolds seeded with MSCs were placed in non-tissue culture treated plates, the media aspirated and the fibrin-MVF gel was infiltrated into the pores of the HA by pipetting. For the control group, the 125 μ L of fibrin containing MVFs was cast above the culture of MSCs in the well plate. For all groups, the fibrin gel was allowed to completely gel before the addition of co-culture media. Co-culture media was composed half of vessel growth promoting media and half osteogenic induction

media. Vessel growth media consisted of 80% DMEM (Gibco), 20% FBS (ATCC), and 1% PSA (Gibco). Osteogenic media consisted of 96% DMEM (Gibco), 3% FBS (ATCC), 1% PSA, 50 $\mu\text{g/mL}$ L-ascorbic acid, 10 mM β -glycerophosphate, and 10 nM dexamethasone. Mycozap (Lonza) was added 1 mL per 500 mL media. To decrease fibrin contraction, 6-aminocaproic acid was added at a concentration of 1 mg/1 mL of media. Media was used within 7 days due to the instability of certain components in the osteogenic induction media.

Media samples were collected at 1, 3, 7, 10, 14, 17 and 21 days. The supernatant media was collected for alkaline phosphatase (ALP; $n = 5$ replicates) and calcium colorimetric (Ca^{2+} ; $n = 5$ replicates) analyses according to manufacturer's instructions (Sigma Aldrich, St. Louis, MO). Biological samples for imaging and RNA sequencing were stopped after 3, 7, 14 and 21 days of culture. Biological samples were fixed with Trizol, homogenized for RNA extraction ($n = 5$ or 6 replicates), and then frozen. RNA was extracted using RNeasy Kit (Qiagen, Hilden, Germany) following the manufacturer's protocol. RNA concentration and quality was evaluated using a Take3 Micro-Volume Plate (Biotek, Winooski, VT) and a spectrophotometer. RNA samples of adequate quality for sequencing, at $> 50 \text{ ng}/\mu\text{L}$ concentration and 3 biological replicates per group per time point, were used to prepare sequencing libraries according to the manufacturer's RNA sample protocol (Illumina, San Diego, CA). These prepared libraries were then barcoded, pooled, and sequenced in an Illumina HiSeq 3000 to generate 50 bp single end reads with sequencing depths of 45 million reads on average. Reads were aligned using a TopHat2 aligner mapped to *Rattus norvegicus* rn6 genome build.³⁰ HTSeq was used to transform alignments to raw read counts per gene.¹

Immunohistochemistry (IHC)

Biological samples of *in vitro* culture from each group tested and time point ($n = 3$ replicates/group/time point) were fixed using 4% formaldehyde and permeabilized with 0.5% Triton X-100, stained with Rhodamine-labeled Griffonia (Banderiaea) Simplicifolia Lectin I (GS-Lectin, Vector Labs, Burlingame, CA), which is a carbohydrate-binding protein that stains the vessel wall. The cultured scaffold samples then underwent a decalcification procedure to dissolve the HA content of each scaffold. Scaffolds were decalcified by immersing in 4% formic acid and with gentle agitation at 25 °C for 1–2 days, until the HA scaffold dissolved as observed by reduc-

tion in each sample opacity. After decalcification, the fixed biological samples were re-stained using GS-lectin and were imaged using a TCS SP8 confocal microscope system (Leica Camera, Wetzlar, Germany). Samples were imaged at 10x magnification with a z-stack projection; at least 3 regions of interests (ROIs) were selected per group. The size of each ROI was $780 \times 780 \mu\text{m}$. The total length of vascular fragments within each ROI were calculated by traced centerline length measurement using ImageJ (U.S. National Institutes of Health, Bethesda, MD)⁶⁴ and tabulated for comparison between groups.

Experimental Hypotheses Testing

Based on the differences between samples observed in the vascular development, two additional experimental hypotheses were evaluated: (1) since the 250 μm and fibrin gels demonstrated similar vessel patterns, differences in gene expression between those two groups of the RNASeq was modeled across time, and (2) to identify specific differences between the scaffold groups based on pore size, since the only differences in the RNASeq analysis were observed at Day 7, a specific comparison between the scaffolds (450 vs. 340 vs. 250 μm) was conducted based on a sub-analysis of the same RNASeq data at day 7 to highlight significant differences. Pathway enrichment analysis was performed using the clusterProfiler package in R to assess the biological significance of these significantly altered genes.

Finite Element Modeling of Blood Vessel Growth

The μCT scans of the scaffolds (as described in Sect. 2.2) were resized by a factor of four in Ctan (Bruker) with a resulting resolution at 35.08 μm per image. Scans were imported as image stacks into ImageJ and a region of interest (ROI) of a size of $50 \times 50 \times 50$ pixels was selected. The selected region consisted of two components: the scaffold and the negative space which was representative of the fibrin gel loaded with MVFs. The final size of the representative region modeled, was a cube with 1.754 mm side. The respective control was a fibrin gel of a size of 1.754 mm (which represented an infinitely large pore). Each representative volume was then imported to Mimics (Materialise NV, Leuven, Belgium) for volumetric meshing.

Volumetric tetrahedral meshes were formed within Mimics for the control and scaffolds of each pore size. Within Mimics, a series of refinements were performed including correction of planar holes, flipping inverted

elements (so that element normal were congruent), and shell reduction with volumetric conservation (to provide a more accurate mesh). Refined meshes were subsequently imported into Abaqus (Dassault Systems, Johnston, RI) to convert these meshes into geometric meshes. Conversion was accomplished by running a python script and allowing for the conversion of the exported tetrahedral mesh into an 8-node hexahedral mesh.

Each hexahedral mesh was imported into AngioFe, a plugin of FEBio (University of Utah, Salt Lake City, UT) to run simulations.¹⁷ Meshes were imported to PreView (University of Utah, Salt Lake City, UT) and boundary conditions, time steps, and material properties were assigned.⁴⁴ The following values were used for material parameters: (a) per single sprout as 3.72 μPa , sprout stress range (b) as $1/250 \mu\text{m}^{-1}$, sprout stress width (cosine exponent) (N) as 2, microvessel constitutive mode-modulus (E_{vess}) as 3.452 kPa, ECM constitutive model-stiffness of ground matrix (E_M) as 34.52 Pa, ECM constitutive model-nonlinear fiber stiffness (E_{fib}) as 345.2 Pa, and ECM constitutive model-viscoelastic time constant (τ) as 1.08 s.^{16,17,33} Rigid constraints were applied along nodes to simulate the interface between the gel and scaffold appropriately. In order to mimic the contact between the fibrin gel and HA scaffold, the interior free surface nodes were constrained in all directions to represent gel attachment to the scaffold surface. The exterior nodes were left unconstrained to represent free surfaces of the gel. Time stepping parameters were set at 20 steps with a step size of 0.1. The material properties of the model were a combination of microvessel (a neo-Hookean material)⁴⁵ and extracellular matrix materials (ellipsoidal fiber diameter neo-Hookean).⁵⁰ Seeding of 20 MVFs within the construct was performed using a random number generator for stochastic simulation. The resulting analyses were run using SHAMU, a high performance computing cluster; the simulations were run in batches within a parallel environment. In order to determine how pore size effected rate of growth, angiogenesis was simulated over 7 days in terms of time stepping (in terms of simulated vessel growth rate). The results of the runs were visualized in PostView and total vessel length and number of blood vessel branches was extracted from each run. Each architecture (450, 340 and 250 μm pore size and fibrin) were between 30 (for 450 μm pore size) to 11 times (for fibrin hydrogels) with random seeds to allow the final blood vessel lengths and branching to converge with a confidence of $> 90\%$. In addition, three independent scaffolds (of the same pore size) regions of interest were modeled and evaluated to ensure that the local geometric choice was not a confounding variable.

Statistical Analyses, Gene Set Analyses and Differential Expression

Statistical analyses (for calcium colorimetric assay, ALP, and blood vessel length) was performed in SigmaPlot 13 (SyStat, San Jose, CA) via the two-way ANOVA design and using Tukey testing *post hoc*. Statistical significance was designated at $p < 0.05$.

Statistical analysis of differential expression was performed using DESeq2⁴³ package on the R platform,⁷³ starting from the read counts for each gene in each sample. The scaffold (four different types: Fibrin, 450 μm , 340 μm , 250 μm) and duration (four different lengths of *in vitro* culture: day 3, 7, 14 and 21) were treated as independent categorical variables in the design matrix. Log-fold change values were adjusted using apeglm⁸⁰ method to estimate shrinkage of effect size. P-values were calculated using the Wald test. For the specific gene trend panels, significant differences on normalized counts were conducted using two-way ANOVA with tukey's test used to determine *post hoc* significance ($p < 0.05$).

For more detailed interrogations, the following comparisons were made: (i) 250 μm vs. fibrin across time, (ii) comparison between the scaffolds (450 vs. 340 vs. 250 μm) at day 7 of *in vitro* culture. Significant hits (adjusted p value < 0.05) were extracted and arranged by log fold change. Gene ontology (GO) gene sets, specifically C2 GO Biological Processes genesets and KEGG pathway genesets, were downloaded from the MSigDB database.⁴² Gene set over representation and enrichment analyses, and visualizations were performed using clusterProfiler⁷⁹ and WebGestalt.⁴¹

RESULTS

Scaffold Characterization

SEM evaluation revealed an open, porous interconnected structure (Fig. 2a) of the HA scaffolds that potentially allows for tissue ingrowth. Scaffold porosity was $91.2 \pm 0.8\%$ for the 450 μm , $88.4 \pm 1.5\%$ for the 340 μm , and $86.6 \pm 2.6\%$ for the 250 μm pore size scaffolds, respectively (Fig. 2b). The porosity was of the three scaffold types tested in the present study was similar. The permeability of the scaffolds was measured at $9.4 \pm 5.9 \times 10^{-10} \text{ m}^2$, $5.0 \pm 3.3 \times 10^{-10} \text{ m}^2$ and $2.4 \pm 1.9 \times 10^{-10} \text{ m}^2$ for the 450, 340, and 250 μm pore size scaffold respectively (Fig. 2c). The permeability was significantly reduced when the pore size was reduced from 450 to 34 to 250 μm ($p < 0.05$, each group from the other). The measured structural indices from SEM (strut thickness and strut separation) and μCT (9 histomorphometric parameters) are listed in Table 1. The nomenclature for the scaffolds, namely

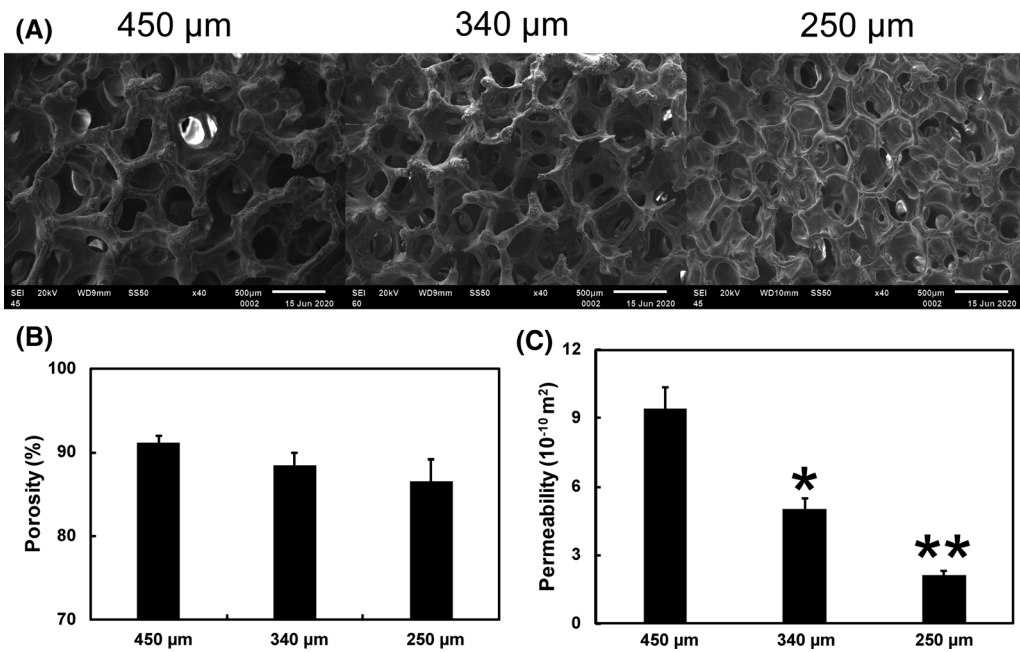


FIGURE 2. HA scaffold architectures and porosity. (a) SEM images of 450, 340, and 250 μm pore sized HA scaffolds indicating measurement of strut length and thickness. (b) Porosity measured by helium pycnometry for each pore size indicating no significant differences ($n = 6/\text{group}$). (c) Fluid permeability of each pore size indicated that the permeability of each of the larger pore sizes was significantly greater than each of the smaller (*, ** indicates significance at $p < 0.05$ from other groups, $n = 6/\text{group}$).

TABLE 1. Architectural characterization of the hydroxyapatite scaffolds.

	450 μm	340 μm	250 μm	
Strut spacing	424.98 ± 178.9	359.85 ± 69.6	211.71 ± 43.5	μm
Strut thickness	842.33 ± 14.3	95.90 ± 24.2	64.07 ± 19.5	μm
Scaffold vol/tissue vol	11.32 ± 0.9	16.06 ± 2.8	21.05 ± 3.8	%
Scaffold surf/scaffold vol	31.25 ± 1.1	33.86 ± 6.3	38.38 ± 4.6	1/mm
Scaffold surf/tissue vol	3.53 ± 0.2	5.42 ± 1.5	7.94 ± 0.4	1/mm
Trabecular pattern factor	-10.44 ± 1.4	-2.73 ± 4.3	4.98 ± 2.9	1/mm
Structural model index	-0.85 ± 0.2	0.22 ± 0.8	1.15 ± 0.23	
Trabecular thickness	98.96 ± 3.0	100.84 ± 11.6	96.11 ± 11.56	μm
Trabecular number	1.14 ± 0.1	1.59 ± 0.2	2.18 ± 0.1	1/mm
Trabecular separation	842.33 ± 14.3	526.10 ± 80.9	316.88 ± 9.9	μm
Degree of anisotropy	1.21 ± 0.0	1.22 ± 0.1	1.24 ± 0.1	

Strut thickness and spacing are calculated from scanning electron microscopy, all other metrics are from microcomputed tomography analysis.

$n = 6$ scaffolds per architecture minimum.

Vol volume, Surf surface area.

450, 340, and 250 μm instead of 45, 60 and 80 pores per inch of the template foam, respectively, was chosen from the strut spacing measurements, which correspond to the opening sizes between pores.

Calcium and ALP Content in the Supernatant Media

The calcium (Ca^{2+}) concentration levels of all groups are shown in Fig. 3a. For all groups tested, the

in Ca^{2+} levels peaked at day 3 ($24.1 \pm 3 \text{ nmol}/\mu\text{L}$) but subsequently decreased after day 3 of the study. The Ca^{2+} levels were significantly ($p < 0.001$) lower by Day 14 from Day 3 ($p < 0.001$). Overall, samples with 450 μm pores had the lowest media Ca^{2+} levels throughout the duration of 21 days (significantly lower than 340 μm pores, $p = 0.048$ and the 250 μm pores, $p = 0.028$, and lower than but not significantly different compared to fibrin at $p = 0.389$).

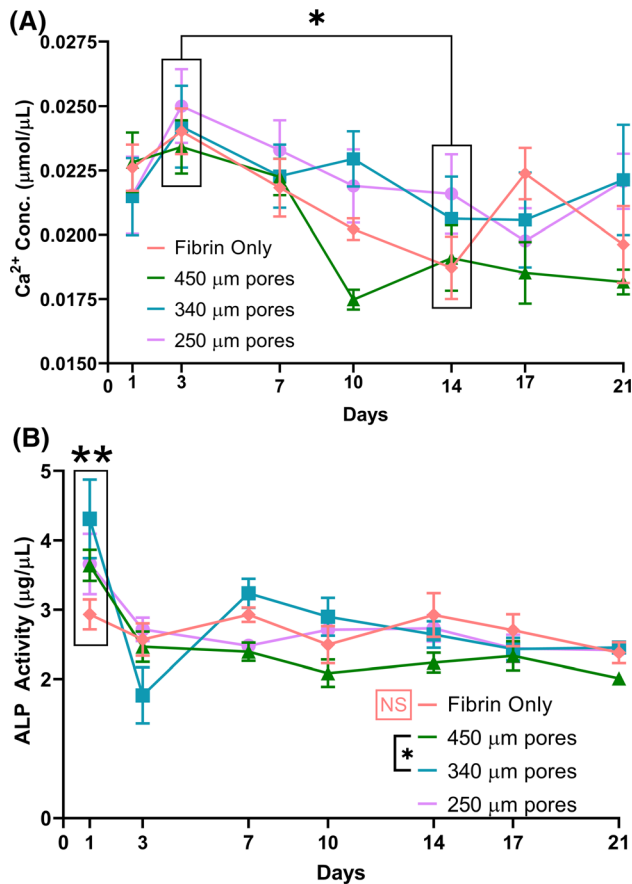


FIGURE 3. Media Ca^{2+} and ALP expression. (a) Calcium concentrations. Media Ca^{2+} was significantly higher at day 3 compared to day 14 (*, significant at $p < 0.001$, main effect across groups, $n = 5/\text{group}/\text{time point}$). (b) ALP activity. Significantly greater ALP in the 340 μm group compared to the 450 μm (* $p = 0.026$, main effect across time). Significantly greater ALP was observed in all groups at Day 1 (**, main effect, $p < 0.001$). There was no significance between timepoints within fibrin only group (orange NS, $p > 0.67$). $n = 5/\text{group}/\text{time point}$.

Alkaline phosphatase activity (ALP) (Fig. 3b) peaked ($3.87 \pm 1.0 \mu\text{g}/\text{mL}$ across HA groups) at Day 1 and was statistically significant ($p < 0.001$) from other durations of *in vitro* culture, as a main effect independent of scaffold group. No substantial increase was observed in ALP in the fibrin group at Day 1 ($2.93 \pm 0.5 \mu\text{g}/\text{mL}$, compared to $2.70 \pm 0.6 \mu\text{g}/\text{mL}$ for all other days, $p > 0.668$). After day 3, ALP activity decreased and leveled off for the remainder of the study for all scaffolds ($2.47 \pm 0.6 \mu\text{g}/\text{mL}$ across HA groups on all other days, no significant difference between any group at any time point, Day 7 $p > 0.085$, Day 10 $p > 0.08$, Day 14 $p > 0.183$, Day 17 $p > 0.7$, Day 21 $p > 0.6$). ALP expression was significantly different ($p < 0.05$) between samples with 450 μm pores and 340 μm pores ($p < 0.05$) across all timepoints and, at day 1, expression was different between samples with 340 μm pores and fibrin

($p < 0.001$) and at Day 3 between the scaffolds with 340 μm pores and 250 μm pores ($p = 0.027$). Significant ($p < 0.05$) difference, in the ALP expression was obtained at day 1 for both the 450 and 340 μm pore scaffolds within their respective groups. Scaffolds within the fibrin only were similar for all timepoints. Detailed statistical analyses for Calcium and ALP content are available in the supplemental data.

Osteogenic Differentiation and Mechanotransductive Signaling

The principal components analysis from the RNA-Seq study indicated that there was a clear distinction between the response of the HA scaffold groups, compared to the fibrin control over 21 days (Fig. 4a). No distinctions were seen along the principal component axes between the different pore sized scaffold groups themselves at any given time point. On day 3 and day 7 groups, all materials tested were significantly different from each other and from the Day 14 and Day 21 groups. The latter time points overlap to the extent of being indistinguishable (Fig. 4a). The correlation heatmap suggested that the trends in gene expression were similar for the results obtained when the cells were cultured in the 450 μm , 340 μm and 250 μm HA scaffold and distinctly different from the fibrin group over 21 days (Fig. 4b).

Expression of genes pertinent to osteogenesis highlighted differences between MSC differentiation on the fibrin and the scaffold groups (Fig. 5). Expression (normalized counts) of genes encoding BMP2 and Osteopontin (*spp1*) were all much higher when the cells were cultured in the HA scaffold groups at early time points compared to those cultured in the Fibrin group, but the expression levels of cells in all the groups match for all times after Day 7. In the case of *bmp2*, expression in the 450 μm group was higher than all other groups, $p < 0.001$ and expression in the 250 and 340 μm groups was higher than fibrin at $p < 0.014$ at Day 3, while expression in the 340 μm group was higher than all other groups at Day 7, $p < 0.01$. In the case of *spp1*, expression was significantly different between all groups except the 450 and 340 μm groups at Day 3, $p < 0.01$ and significantly different between all groups except 250 and 450 μm groups at Day 7, $p < 0.001$. Since calcium signaling was identified as a pathway that had multiple genes with significant differential expression, the gene encoding calmodulin was investigated and showed that its expression when cells were cultured in the fibrin group was consistently higher, significantly different from all scaffold groups (main effect, $p < 0.001$) but no significant differences were found between the scaffold groups (except between 340 vs. 250 μm , $p = 0.039$). *Yap/Taz* have

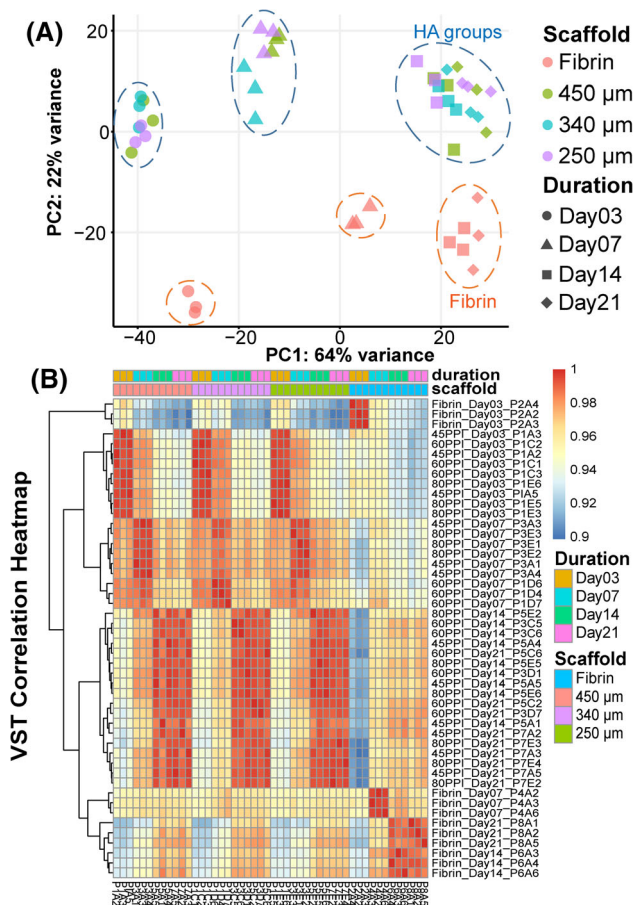


FIGURE 4. Differences between the scaffolds and fibrin over time. (a) PCA of the RNA Seq analysis for the various conditions tested within the experimental design (4 scaffold groups \times 4 time points), showing a clear separation between the fibrin (circled with orange dashed lines) and the HA scaffold based groups (circled with blue dashed lines). Temporal trends were similar in all groups, with Day 3 and Day 7 (circled separately) being functionally distinct compared to Day 14 and 21 samples (combined within circles) ($n = 3$ per scaffold per duration). (b) Correlation heatmap of the various conditions tested confirming the PCA analysis. Hierarchical clustering was performed across samples along the Y-axis. The first 3 column blocks of scaffold, show the HA scaffold correlations being very similar and distinctly different from the last column block (fibrin).

been implicated in the HIPPO mechanotransduction pathway and while the trends for these genes over time were the same in all scaffold groups, *Taz* was consistently lower in scaffolds compared to fibrin (significant for each scaffold vs. fibrin, $p > 0.032$) and the expression level of *Yap1* was consistently higher in scaffolds compared to fibrin (significant for each scaffold vs. fibrin, $p < 0.011$). Wide variations over time (days 3 and 7 significantly higher than days 14 and 21, $p < 0.009$) and no difference between groups ($p > 0.698$) was observed in *tgfb1* expression. The gene encoding osteonectin, *sparc* also exhibited no

differences between scaffold groups, but Day 3 expression was much higher than all other time points across groups ($p < 0.011$). The opposite trend was observed where *runx2* and *colla1* expression was initially low, (*runx2* Day 3 was significantly lower than all other time points $p < 0.001$, while *colla1* Days 3 and 7 were significantly lower than later time points, $p < 0.006$) and then increased towards the end of the study, indicating continuing promotion of osteoid formation (Fig. 5).

Vascular Growth Within the Hydrogel and HA Scaffolds

Growth of the MVFs in fibrin gel and HA scaffolds were evaluated by confocal imaging using a tagged GS-Lectin to stain the vessel wall (representative images in Fig. 6a). The results revealed that the MVFs were dispersed and short (28–35 μm in size) at day 3, but had grown significantly in length by day 7. The lowest vessel length measurement on day 7 (74 μm) was in the 250- μm -pore size scaffold while the longest vessel fragments (140 μm) were found in fibrin-only group. The 450- μm and 340- μm scaffolds showed a trend of supporting mild vessel growth from day 7 to day 14 and 21, while the fibrin group similarly showed relatively little change in vessel length between day 7 and day 21 (Fig. 6b). The 250- μm scaffolds demonstrated steady increase in vessel length from day 3 to day 7 to day 14 before vessels stabilized in length for the final 7 days of observation. Interestingly, the MVFs in the 450- μm scaffold exhibited looping, structures of larger tubes, with smaller branches growing from them, in the morphology of and on the same scale as individual pores of the 450- μm size. This effect was evident at day 7 and prominent at day 14. Both the fibrin and 250- μm size scaffolds showed long branched vessels forming from the MVFs, but explicit evidence of network anastomoses between vessels was limited in both groups. These distinct phenotypes are schematically represented in Fig. 6c. The 340- μm pore size scaffolds showed a mixture between some vessel fragments looping within pores and some branching across pore interconnections by days 14 and 21. At day 21, MVF growth exhibited a delineation of tubular structure. It was also observed that individual cells (GS-lectin stained) were migrating away from the fragments by the 21 day observation time point.

Vascularization and Hypoxia Signaling

Evaluation of genes of importance to in angiogenesis and blood vessel network organization highlighted differences between the fibrin and the scaffold groups tested in the present study (Fig. 7). The expression (normalized counts) of genes encoding Angiopoietin 2

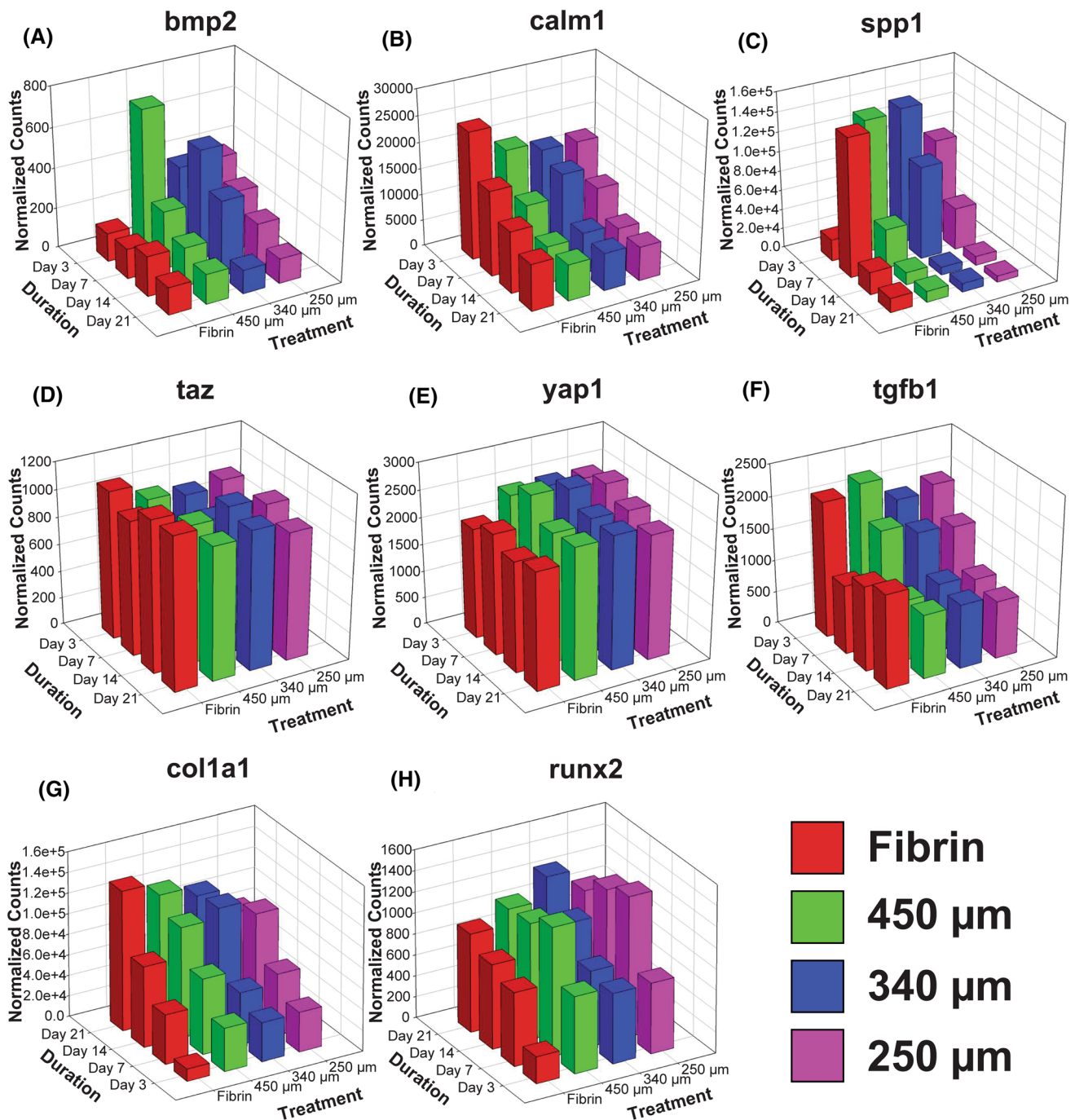


FIGURE 5. Osteogenic gene evaluation. (a–f) The graphs depict average normalized counts (across 3 samples) of indicated gene regulators of osteogenic differentiation across the four time points from Day 3 to Day 21 for the different experimental treatments. (g, h) The graphs depicting average normalized counts (across 3 samples) of early osteogenic gene markers (*col1a1* and *runx2*) across the four time points, plotted from Day 21 to Day 3 to enable visualization. (All significant differences in supplementary data table, $n = 3$ per scaffold per duration).

was higher for the fibrin group compared to the scaffolds ($p < 0.001$, main effect). However, the trend was reversed for Angiopoietin 1, *serpine1* (the gene encoding plasminogen activator inhibitor), *camk2*

(gene encoding calmodulin dependent protein kinase) and *tek* (gene encoding the Angiopoietin 1 receptor) were much higher in the scaffold groups compared to the Fibrin group (main effect, $p < 0.001$). This

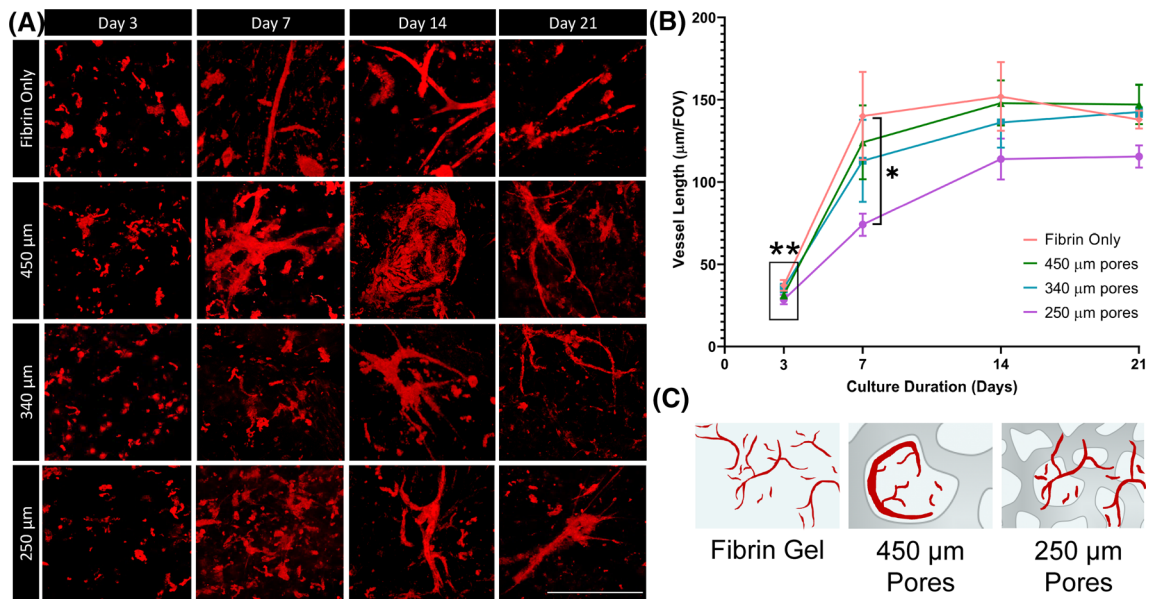


FIGURE 6. MVF growth over time. (a) Microvascular fragment growth was tracked after 3, 7, 14 and 21 days in the fibrin hydrogels and the decalcified 250 μm, 340 μm and 450 μm pore size scaffolds. Confocal IF imaging of samples stained with GFP conjugated GS-Lectin. The most distinctly different morphologies were observed after 14 days of culture (Scale bar 500 μm). (b) All groups showed increase in length measured from day 3 to day 14 followed by stabilization of length to day 21 (** indicates day 3 significantly lower than other times, $p < 0.001$ and * indicates fibrin significantly different from 340 μm group at Day 7, $p = 0.011$). 3 independent biological measures with at least 4 independent regions were measured at each time point for each group. (c) Schematic showing the morphology of vessels in the fibrin hydrogel and 250 μm pores being similar while the morphology in the 450 μm pores was distinctly different.

shows that vessel stabilization in the scaffolds followed stabilization *angpt1* rather than *angpt2*. The *angpt2* gene was highly expressed both early (day 3) and late (days 14 and 21) in the Fibrin group compared to all the HA groups tested ($p < 0.001$). There were significant differences in *hif1a* and *vegfa* expression between the 450 μm and 250 μm scaffolds vs. Fibrin ($p < 0.001$) but not between the 340 μm scaffolds vs. Fibrin ($p > 0.087$), the hypoxic response was much more pronounced in terms of significantly higher *hif1a* expression in all the scaffold groups compare to respective results obtained from the Fibrin group. This outcome was supported not just by changes at the single gene expression level, but across the HIF-1 signaling pathway, which revealed that several genes (encoding IL-6, HIF1α, camk2, serpine1) indicating either sustained or continuous hypoxia were significantly upregulated across HA scaffold groups compared to Fibrin, while genes in the intermittent hypoxia pathway (encoding NOX, PLCγ, PKC) were significantly upregulated in the Fibrin group over the scaffolds (data not shown). The upregulation of angiopoietins was observed differentially, but was upregulated across the protein class in all groups. This

outcome supported the blood vessel development observed in Fig. 6a across all groups over time.

Differences between Scaffolds with small pores and Fibrin hydrogel

The morphology of the vessels in the 250-μm pore size scaffolds exhibited similar morphology in the fibrin hydrogel, especially after 14 days of culture (Fig. 6c). A heat map comparison of genes involved in osteogenesis between the two groups over time shows that BMP2 was upregulated early (day 3 and day 7) in the 250-μm scaffolds compared to Fibrin (Fig. 8a). The early markers of osteogenic commitment (*runx2*, *coll1a1*) were upregulated at day 14 and 21 in the scaffold group, while they were upregulated in the fibrin group at day 21 only. Similarly, *spp1* (that encodes osteopontin) was upregulated in 250 μm scaffolds at day 3, ahead of upregulation in fibrin at day 7.

In terms of significantly altered gene sets, it was observed that both hypoxia and mechanotransduction were significantly upregulated in the scaffold compared to fibrin at a significant level of overrepresentation. Cell adhesion molecule pathways, chemokine and cal-

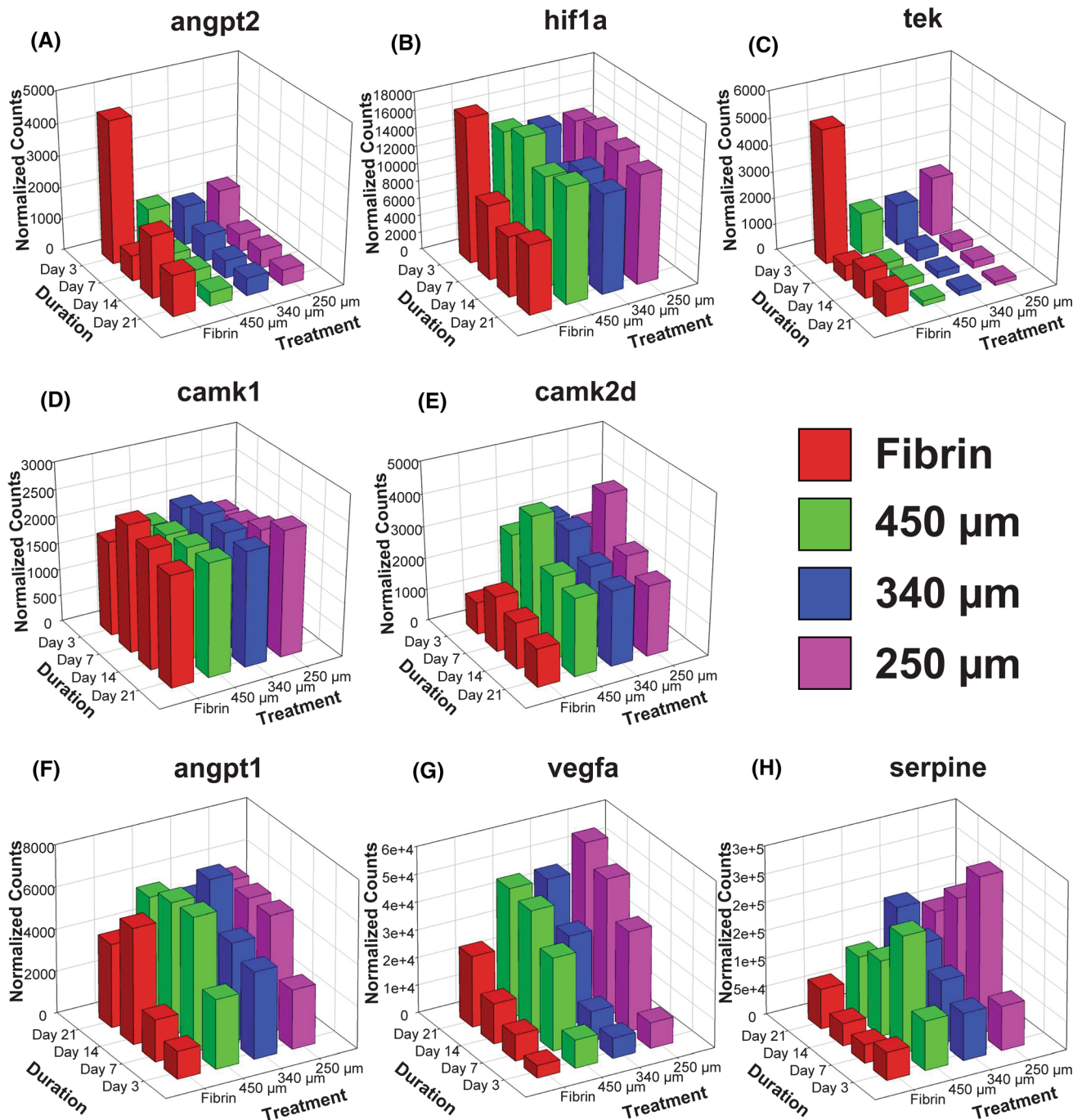


FIGURE 7. Angiogenic gene evaluation. (a–e) The graphs depict average normalized counts (across 3 samples) of indicated gene regulators of angiogenesis across the four time points from Day 3 to Day 21 for the different experimental treatments. (f–h) The graphs depicting average normalized counts (across 3 samples) of gene markers of angiogenesis (angpt1, vegfa and serpine) across the four time points, plotted from Day 21 to Day 3 to enable visualization. (All significant differences in supplementary data table, $n = 3$ per scaffold per duration).

cium signaling were down-regulated in the scaffold group compared to fibrin over 21 days (Fig. 8b). In terms of the angiogenic response, the gene-set enrichment analysis of 250- μm scaffolds vs. Fibrin samples

across 21 days indicated many more genes involved in angiogenesis in terms of rank ordered set of fold change in gene expression are upregulated in Fibrin compared to 250- μm scaffolds (Fig. 8c).

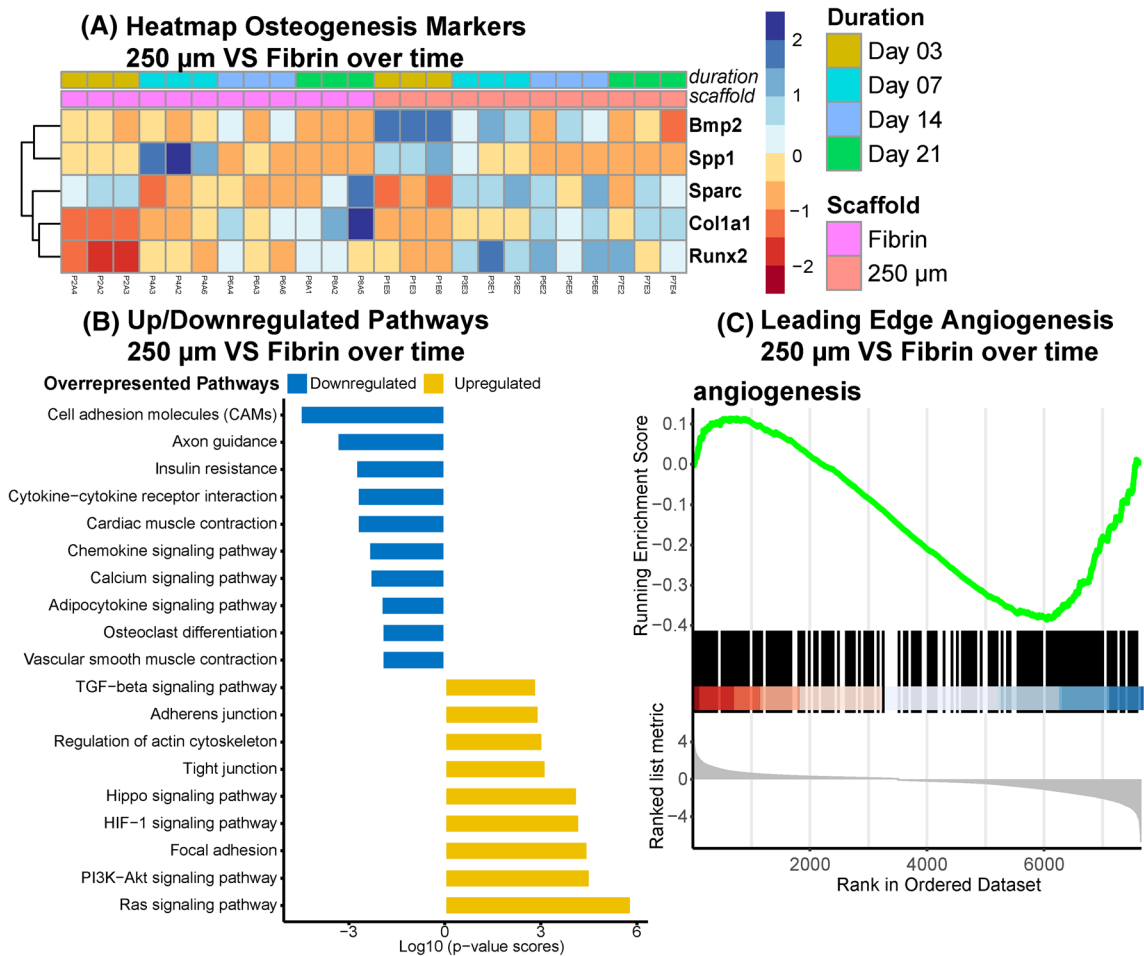


FIGURE 8. Impact of porous hydroxyapatite scaffold. (a) Hierarchical clustering of normalized expression counts of a subset of osteogenesis genes across samples. The samples are color coded by time points (upper bar) and scaffold type (lower bar) at the top of the heatmap (All significant differences in supplementary data table, $n = 3$ per scaffold per duration). (b) Pathway enrichment analysis of the significantly altered genes highlights the most significantly altered pathways (blue: downregulated or yellow: upregulated) between 250 μ m vs. Fibrin. The x-axis plot the significance of overrepresentation. (c) The angiogenesis pathway was a significant hit in geneset enrichment analysis of 250 μ m vs. Fibrin samples across time. The leading-edge graph illustrates the positions of significantly altered genes in our dataset within Angiogenesis dataset in the context of all genes ordered by fold change gene expression. There were distinct subsets of genes (shown by clustering of black bars in the center heatmap band) in the angiogenesis pathway differentially upregulated in 250 μ m scaffolds and in Fibrin.

Vascular Morphogenesis in Scaffolds with Different Pore Sizes

Another distinction of interest was the separation in the principal component analysis evaluating the different scaffold pore sizes alone (250-, 340-, and 450- μ m) at day 7, providing evidence that there were significant differences in the 340- μ m scaffold at the gene level compared to the other two groups (Fig. 9a). Differential gene expression analysis indicated that 1570 of the 1990 genes in the 450- vs. 340- μ m comparison were common to the 2422 significant genes identified between the 250 vs. 340 μ m scaffold groups (Fig. 9b). This observation was also supported by the heatmap of significantly altered genes across scaffold groups at day 7 showing consistencies across the 250-

and 450- μ m pore size scaffold with stark contrast to the 340- μ m pore size scaffold (Fig. 9c). Interestingly, in addition to pathways implicated in cancer (which are often common to fenestrated vasculature development and stromal signaling during the proliferative phase of regeneration), the hypoxia signaling pathway (Hif1 α) and the mechanotransduction pathway (Hippo signaling) were identified as significantly over-represented (Fig. 9d).

Computational Studies of Matrix Mechanics on Vascularization

Figure 10 describes the results from the computational biomechanics modeling which simulated vessel growth in fibrin gels within scaffolds constrained at the

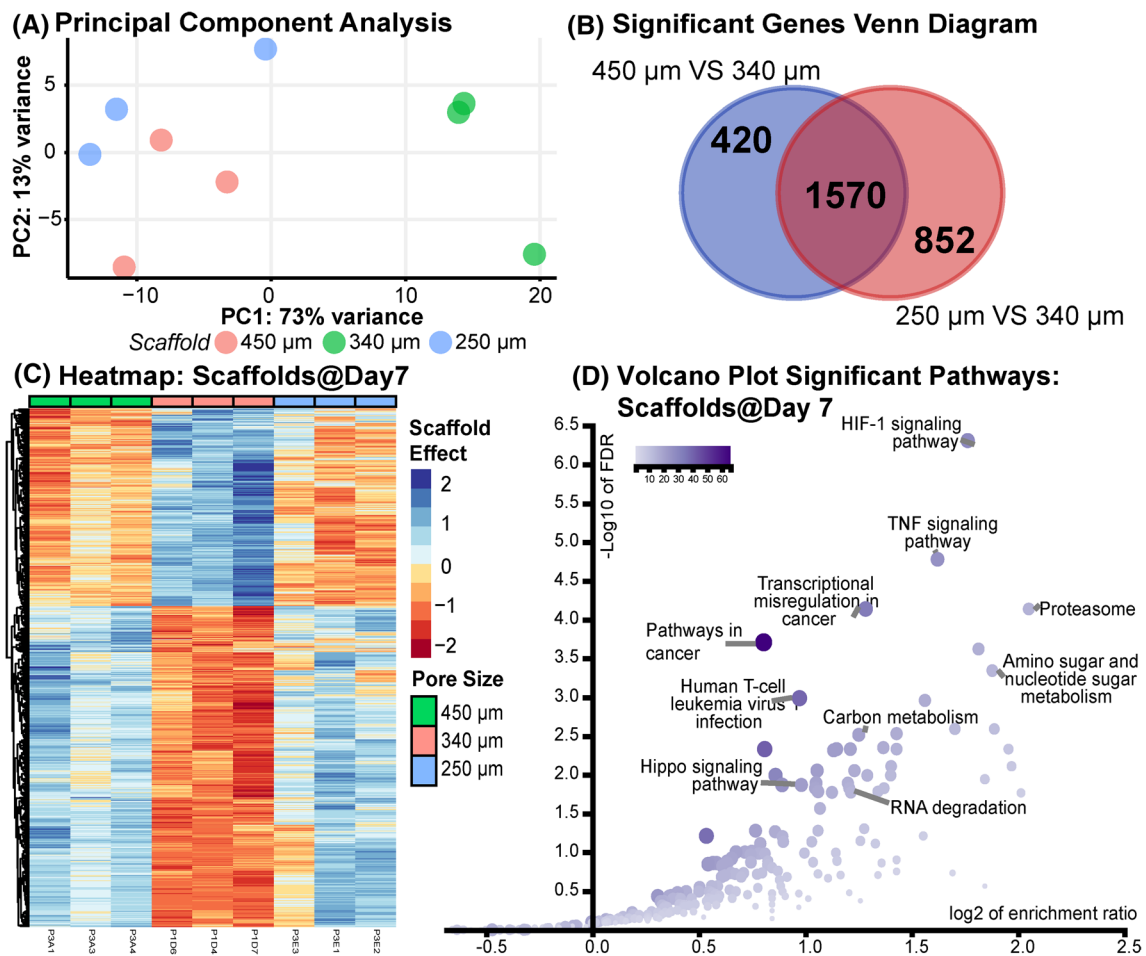


FIGURE 9. Effect of pore size at Day 7. (a) Principal Component Analysis illustrating the separation of the different scaffold groups at Day 7 once fibrin condition was removed. The 340 μm group was significantly different from the other two. (b) Differential gene expression was evaluated for 450 μm vs. 340 and 250 vs. 340 μm scaffold groups and the venn diagram illustrates the common and unique genes within each hit list. (c) Heatmaps of significantly altered genes among the three groups corroborating the difference in 340 μm (center 3 columns) from the other two groups (3 columns on the right and left). (d) The common genes from the venn diagram were used for pathway analysis. The volcano bubble plot illustrates pathways significantly overrepresented in the common hits. The x-axis represents the enrichment score and y-axis plots adjusted p-values of the enrichment.

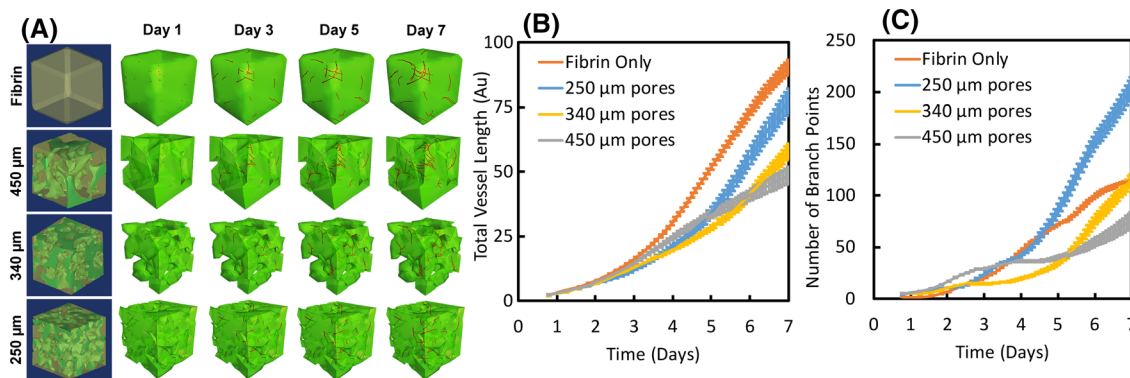


FIGURE 10. Computational vessel growth modeling. (a) 3D models of the pore spaces filled with hydrogel were created for the fibrin control as well as the 250 μm , 340 μm and 450 μm pore size scaffolds and vessel growth was simulated over multiple iterations and regions of interest using the AngioFE plugin over a period of 7 days. Distinct differences in (b) Total vessel length and (c) Number of branch points were observed between the groups over 7 days, without significant variations within a given group (variations might have resulted from region of interest selection or random seeding, $n = 7$ per architecture per time point.)

scaffold-gel interface, resulting in a strain field in the gel which affected vessel growth. During the seven day AngioFE simulation, the 20 randomly seeded MVFs were observed to grow over a period of seven days between the control, 250- μm , 340- μm , and 450- μm pore (Fig. 10a) and achieving significantly greater lengths at Day 7. The fibrin control exhibited the greatest increase in vessel length followed by the 250- μm pore ($90603 \pm 2578 \mu\text{m}$ and $77533 \pm 4583 \mu\text{m}$, respectively) (Fig. 10b). The total vessel length in the fibrin was twice that of the 450- μm pore ($48706 \pm 3195 \mu\text{m}$). The 250- μm pore displayed the greatest number of branches (204 ± 10) after 7 days and the control displayed no statistical difference compared to the 340 μm pore (115 ± 2 and 115 ± 6 , respectively after 7 days) (Fig. 10c). Across all groups it was observed that the differences in total vessel length over 21 days tracked were proportional to the branching over time within a group. None of the architectures tested exhibited significant anastomoses over time (data not shown; the highest number recorded was 3, most simulations resulted in 0 anastomoses). The total number of simulations needed to achieve convergence for the total vessel length and number of branches for the control, 450- μm pores, 340- μm pores and 250- μm pores was: 11, 30, 18 and 18, respectively (data not shown, not significant at $p = 0.1$).

DISCUSSION

Supporting Osteogenic Differentiation and Matrix Deposition

The fluid conductance of a bone scaffold was suggested to be critical to the revascularization⁵⁸ and *in vitro* success of graft integration by promoting cell and vessel invasion into the scaffolds. In the bone fracture healing cascade, this is followed by bone in-growth, long term remodeling, and tissue regeneration.⁶⁰ In a rabbit model,²⁸ it was suggested that a minimum threshold conductance of $1.5 \times 10^{-10} \text{ m}^3\text{s}^{-1}\text{Pa}^{-1}$ was necessary and that revascularization and formation of osteoid and fibrous tissue were not achieved below the conductance threshold value. Based on their permeability (equivalent to conductance ranging between 8.82×10^{-10} and $49.95 \times 10^{-10} \text{ m}^3\text{s}^{-1}\text{Pa}^{-1}$) the HA scaffolds investigated in this study were all well above the threshold values, suggesting the ability of these scaffolds to promote and sustain bone in-growth and regeneration. This is supported by the patent growth of cells within

the scaffolds in addition to MVFs until day 21 *in vitro* without dynamic perfusion and despite increasing metabolic demand. While continuous hypoxia is upregulated in the scaffolds, pro-angiogenic signaling was also activated, indicating a system continuing toward homeostasis (Fig. 5).

In human bone, permeability has been implicated in the complex interplay between the remodeling mechanical responses of cortical and cancellous bone *via* the poroelastic models,¹⁰ suggesting that response to fluid shear and the mechano-transduction of pertinent signals were through fluid–solid coupling. The permeability of the scaffolds used in this study, especially the 340- μm pore size scaffolds, was comparable to the permeability of human bone in the femur.⁵¹ Permeability was also identified as the critical factor affecting nutrient and calcium transport.³¹

In terms of the temporal sequence of osteogenesis, the scaffolds benefit from early upregulation of BMP2 (unlike *tgfb1* which was high across all groups and fibrin gels at day 3) calmodulin and osteopontin, and later RUNX2 and Collagen type I, which likely resulted in local remodeling supporting further MSC commitment to the osteogenic lineage. This is likely due to secretion from the MVFs, which being freshly isolated might “behave” like a local injured vascular bed supporting both MSC recruitment and niche specific differentiation. Several publications suggest that the wound-site vasculature, especially within a fibrin blood clot, (which the hydrogel in the biphasic system of the present study represents) are a prime source of BMP2^{47,77} The RUNX2 upregulation may then be explained as an MSC response to the early mitogenic and strong differentiation signal of BMP2 (Figs. 3c and 6a). This outcome is further supported by lack of early ALP activity observed in the Fibrin only group which does not seem to promote a wound healing response that is bone niche specific, like the strong attachment to hydroxyapatite surfaces promotes in MSCs.^{14,49} In terms of the other temporal markers of osteogenic maturation, published reports have noted that expression of non-collagenous maturation-linked proteins (such as Osteopontin (*spp1*)) was linked to mature osteoblasts resident near mature bone mineral⁷⁶ (which is what an HA scaffold approximates), while in other reports, it was also expressed prior to initiation of an osteogenic response in post- marrow ablation treated animals.⁷¹ The early expression of *spp1* seen in all groups might thus be linked to some form of dysfunction in anticipated signaling such as dysfunction in the inflammatory response seen *in vitro* post ablation (Figs. 3c and 6a).

Supporting Blood Vessel Growth and Patterning

Edgar *et al.*¹⁹ have recently noted that the local microenvironment, specifically the mechanical interaction between MVFs and their surrounding extracellular matrix, regulates the rate of neo-vessel growth and branching. The present study as well, provided evidence that over similar volumes, the nature of blood vessel growth and branching was very different between the different scaffold architectures because the boundary constraint of the hydrogels not only being unable to separate from the scaffold surface, but also having steeper stiffness gradients closer to the scaffold surface. The sparse strain field of the 450 μm pore size is likely responsible for the vessels growing within the pores preferentially to find lower matrix stiffness, while due to the lower stiffness regions being relatively more abundant in the pore interconnections rather than the pore interior (smaller pores, greater interconnection density per unit volume) of the 250- μm pore size (Fig. 4). This is also supported by the computational mechanics model where there is early branch formation in the 450- μm pore size scaffolds but, since both the seed vessel and daughter branches stay confined to a single pore, their successive branching is inhibited. Counterintuitively, as the 250- μm pore size scaffolds have MVFs initially lengthening across pores, the future daughter branches also resolve across pores in the computational model (Fig. 8a and 8c), resulting in greater branching and, hence, greater total length over time.

The predictive value of the AngioFE model to simulate MVF growth (Fig. 8) with experimental validation (Fig. 4) is meaningful. Biomaterial scaffold architectures vary based on material, manufacturing process, and desired pore sizes. A tool which allows rapid in silico prediction of vascularization will be essential for narrowing down scaffold design variables for further translation. Such a tool also allows for comparison of architectures from various biomaterials scaffolds using a consistent benchmark to explain whether differences in experimental outcomes have a structural basis. Although many models delve into the biological and biochemical signaling processes behind vascularization, the mechanical forces in the matrix and their specific effects on angiogenesis, and stromal morphogenesis are poorly understood.

Tissue stromal cells secrete paracrine factors and, thus, play a critical role in stimulating angiogenesis. The fact that MVF function is independent of tissue of origin, (despite significant differences in stiffness of those tissues⁵²), indicates that vasculature itself may not be inherently tissue-committed: non-vascular cells may assign tissue-specific function to vascular beds. The local distribution of stromal cells is also capable of

establishing local chemical gradients and, thus, overcome limited diffusion by globally dense matrices.²¹ In the current study, higher levels of pro-angiogenic genes, *vegfa*, *angpt1* and *hif1a*, were expressed within the HA scaffolds that plausibly had more osteogenically committed MSCs (Fig. 5a). Additionally, recent reports indicate that tissue stromal cells induce/promote neovascular invasion across tissue interfaces.¹² This might be critical in biphasic porous scaffolds filled with hydrogels as well, where stromal cells might establish either the chemical or mechanical signaling stimulus, which initiates/affects vascularization across pore spaces.

Temporal Changes in Hypoxia and Mechanotransduction Towards Multi-tissue Engineering

Both of the pathways implicated as central to the morphogenesis in this study across the different forms of evaluation; namely hypoxia and mechanotransduction, not only happen to play out in a temporally varying manner across the groups; but also are involved in subsequent downstream signaling regulating both vessel and osteogenic development. The YAP/TAZ (Hippo) signaling was implicated in both developmental angiogenesis (activated by VEGF⁷⁵) as well in tissue regeneration to regulate vessel network size control during angiogenesis.⁶ In cases of high mesenchymal density, the Hippo pathway also regulates morphogenetic changes by cytoskeletal regulation.^{13,72} The pathway has also been implicated in recent reports of angio and osteogenesis in soft materials subjected to pressure in bone defects.⁵⁹ In the case of the HA scaffolds, where the scaffold surface encourages high cell density locally, (as indicated by the high metabolic load and hypoxia), the upregulated Hippo pathway likely induced an osteogenic phenotype rather than the traditional endochondral preference because of the local presence of vasculature (Fig. 3) based on temporal trends in osteogenic genes. This is supported by literature reports that the hippo signaling is central to healing in vascularized bone healing models where VEGF is involved (like in all the HA groups tested in this study) and there is another factor supporting an osteogenic phenotype (like matrix stiffness⁵ or BMP2³⁹). Thus, scaffold stiffness and properties similar to that of bone mineral seem to play a critical role in promoting an osteogenic phenotype in addition to vasculature in our biphasic model.

Interestingly, the big differences in terms of the pore size effect of the HA scaffolds was limited to the 7 day time point (Fig. 7). Additionally, the critical difference in terms of the poorer/mistimed angiogenic response in the 340- μm pore size scaffold (Fig. 5a) seems to be

driven by a difference in the hypoxia signaling pathway. This is not surprising because adequate levels of HIF1 α are thought to be indispensable for blood vessel invasion, and avoiding energetic distress as metabolic demand increases drastically during phases of high MSC density during bone formation.⁶⁷ Thus, the hypoxia signaling is not only pro-angiogenic, but also pro-survival⁶⁹ for the two tissue types supported in this study.

Confounding factors in the study include the inherent limitation of *in vitro* cell culture with non-homogenous populations. This is further exacerbated by the fact that MVFs are essentially micro-tissues with cells of multiple lineages, including some which have shown significant plasticity and regenerative potential.⁴⁸ Even in the current study, cells (that stained positive for GS-Lectin) were observed to come off the MVF networks indicating that the MSCs might not be the only cells providing stromal/matrix support in the current model. Additionally, because of this distinctly heterogenous, time-variant cell population; while signaling pathways that are significantly different between groups and conditions can be identified using RNA sequencing, it is not feasible to use these techniques to ascertain causality of actors. Similarly, within the currently developed computational model for vessel growth and morphology, very specific growth rates and matrix properties are considered to model the fibrin gel¹⁸ used within the scaffolds. While these models are the first attempt to specifically model geometric constraints in addition to mechanical boundary variations,³³ they can potentially be more accurate if the time variant stiffness of the gels can also be ascertained and incorporated into the model. The significance of these results remains, however, the implication of the hypoxic signaling variance, early initiation of endogenous chemokine signaling, and sustained mechano-transduction pathways as critical players in how cells take cues from the architecture of composite biomaterial scaffolds to dictate stromal and blood vessel growth.

CONCLUSIONS

The architecture of the pores critically determines the rate of growth and the nature of branching of vascular sprouts, while stromal cells promote hypoxia signaling and secrete chemokines to promote this outcome. Scaffold materials impact stromal cell adherence and mechano-transduction; in the presence of blood vessels brings about early osteogenic commitment on hydroxyapatite. The computational mechanics model implicated local matrix strain fields in dictating lengths of blood vessel growth and impli-

cated scaffold architecture in dictating branching morphology. The mesenchymal stromal cell—microvascular fragment combination is a viable *in vitro* model for investigating vascularized tissue morphogenesis in co-cultures.

ACKNOWLEDGMENTS

This research was supported in part by the National Science Foundation CAREER Award (CBET#1847103), an Image Based Biomedical Modeling Fellowship and UTSA Research Funds (GREAT) to TG, funds from the Lutch Brown Endowment to RB, the USAA Foundation to JLO, NIH SC1DK122578 support to CR NIH GM060655 and 1S10OD021805-01 (RISE training program) support to FMA and CP, UTSA College of Engineering support to EJ, UTSA Graduate School support to GC and SM, CPRIT Award RP160732 and NIH NCATS UL1TR002645 support to YC, and AACR AstraZeneca START grant (18-40-12-GORT) support to AG.

REFERENCES

- ¹Anders, S., P. T. Pyl, and W. Huber. HTSeq—a Python framework to work with high-throughput sequencing data. *Bioinformatics* 31(2):166–169, 2015.
- ²Appleford, M. R., S. Oh, N. Oh, and J. L. Ong. In vivo study on hydroxyapatite scaffolds with trabecular architecture for bone repair. *J. Biomed. Mater. Res. A* 89(4):1019–1027, 2009.
- ³Bai, F., J. Zhang, Z. Wang, J. Lu, J. Chang, J. Liu, G. Meng, and X. Dong. The effect of pore size on tissue ingrowth and neovascularization in porous bioceramics of controlled architecture in vivo. *Biomed. Mater.* 6(1):015007, 2011.
- ⁴Baksh, D., R. Yao, and R. S. Tuan. Comparison of proliferative and multilineage differentiation potential of human mesenchymal stem cells derived from umbilical cord and bone marrow. *Stem Cells* 25(6):1384–1392, 2007.
- ⁵Barreto, S., A. Gonzalez-Vazquez, A. R. Cameron, B. Cavanagh, D. J. Murray, and F. J. O'Brien. Identification of the mechanisms by which age alters the mechanosensitivity of mesenchymal stromal cells on substrates of differing stiffness: implications for osteogenesis and angiogenesis. *Acta Biomater.* 53:59–69, 2017.
- ⁶Boopathy, G. T., and W. Hong. Role of hippo pathway-Yap/Taz signaling in angiogenesis. *Front. Cell Dev. Biol.* 7:49, 2019.
- ⁷Campana, V., G. Milano, E. Pagano, M. Barba, C. Cicone, G. Salonna, W. Lattanzi, and G. Logroscino. Bone substitutes in orthopaedic surgery: from basic science to clinical practice. *J. Mater. Sci.* 25(10):2445–2461, 2014.
- ⁸Chang, C. C., and J. B. Hoying. Directed three-dimensional growth of microvascular cells and isolated

- microvessel fragments. *Cell Transplant.* 15(6):533–540, 2006.
- ⁹Chang, C. C., S. S. Nunes, S. C. Sibole, L. Krishnan, S. K. Williams, J. A. Weiss, and J. B. Hoying. Angiogenesis in a microvascular construct for transplantation depends on the method of chamber circulation. *Tissue Eng. Part A* 16(3):795–805, 2010.
- ¹⁰Cowin, S. C. Bone Poroelasticity. In: *Bone Mechanics Handbook*, edited by S. C. Cowin. Boca Raton: CRC Press, 2001, pp. 231–251.
- ¹¹Dadsetan, M., T. Guda, M. B. Runge, D. Mijares, R. Z. LeGeros, J. P. LeGeros, D. T. Silliman, L. Lu, J. C. Wenke, and P. R. B. Baer. Effect of calcium phosphate coating and rhBMP-2 on bone regeneration in rabbit calvaria using poly (propylene fumarate) scaffolds. *Acta Biomater.* 18:9–20, 2015.
- ¹²Dale, J., L. Krishnan, K. Aliaj, J. Beare, J. Weiss, and J. Hoying. Stromal cells promote neovascular invasion across tissue interfaces. *The FASEB Journal* 31(1 Supplement):682.1, 2017.
- ¹³Deel, M. D., J. J. Li, L. E. Crose, and C. M. Linardic. A review: molecular aberrations within hippo signaling in bone and soft-tissue sarcomas. *Front. Oncol.* 5:190, 2015.
- ¹⁴Dulgar-Tulloch, A., R. Bizios, and R. Siegel. Human mesenchymal stem cell adhesion and proliferation in response to ceramic chemistry and nanoscale topography. *J. Biomed. Mater. Res. A* 90(2):586–594, 2009.
- ¹⁵Dumas, J. E., E. M. Prieto, K. J. Zienkiewicz, T. Guda, J. C. Wenke, J. Bible, G. E. Holt, and S. A. Guelcher. Balancing the rates of new bone formation and polymer degradation enhances healing of weight-bearing allograft/polyurethane composites in rabbit femoral defects. *Tissue Eng. A* 20(1–2):115–129, 2014.
- ¹⁶Edgar, L. T., J. B. Hoying, U. Utzinger, C. J. Underwood, L. Krishnan, B. K. Baggett, S. A. Maas, J. E. Guilkey, and J. A. Weiss. Mechanical interaction of angiogenic microvessels with the extracellular matrix. *J. Biomech. Eng.* 136(2):021001–021001-15, 2014.
- ¹⁷Edgar, L. T., S. A. Maas, J. E. Guilkey, and J. A. Weiss. A coupled model of neovessel growth and matrix mechanics describes and predicts angiogenesis in vitro. *Biomech. Model. Mechanobiol.* 14(4):767–782, 2015.
- ¹⁸Edgar, L. T., S. C. Sibole, C. J. Underwood, J. E. Guilkey, and J. A. Weiss. A computational model of in vitro angiogenesis based on extracellular matrix fibre orientation. *Comput. Methods Biomech. Biomed. Eng.* 16(7):790–801, 2013.
- ¹⁹Edgar, L. T., C. J. Underwood, J. E. Guilkey, J. B. Hoying, and J. A. Weiss. Extracellular matrix density regulates the rate of neovessel growth and branching in sprouting angiogenesis. *PLoS ONE* 9(1):e85178, 2014.
- ²⁰Germain, S., C. Monnot, L. Muller, and A. Eichmann. Hypoxia-driven angiogenesis: role of tip cells and extracellular matrix scaffolding. *Curr. Opin. Hematol.* 17(3), 2010.
- ²¹Ghajar, C. M., X. Chen, J. W. Harris, V. Suresh, C. C. Hughes, N. L. Jeon, A. J. Putnam, and S. C. George. The effect of matrix density on the regulation of 3-D capillary morphogenesis. *Biophys. J.* 94(5):1930–1941, 2008.
- ²²Guda, T., M. Appleford, S. Oh, and J. L. Ong. A cellular perspective to bioceramic scaffolds for bone tissue engineering: the state of the art. *Curr. Top. Med. Chem.* 8(4):290–299, 2008.
- ²³Guda, T., J. Walker, B. Pollot, M. Appleford, S. Oh, J. Ong, and J. Wenke. In vivo performance of bilayer hydroxyapatite scaffolds for bone tissue regeneration in the rabbit radius. *J. Mater. Sci.* 22(3):647–656, 2011.
- ²⁴Guda, T., J. A. Walker, B. Singleton, J. Hernandez, D. S. Oh, M. R. Appleford, J. L. Ong, and J. C. Wenke. Hydroxyapatite scaffold pore architecture effects in large bone defects in vivo. *J. Biomater. Appl.* 28(7):1016–1027, 2014.
- ²⁵Guda, T., J. A. Walker, B. M. Singleton, J. W. Hernandez, J. S. Son, S. G. Kim, D. S. Oh, M. R. Appleford, J. L. Ong, and J. C. Wenke. Guided bone regeneration in long-bone defects with a structural hydroxyapatite graft and collagen membrane. *Tissue Eng. A* 19(17–18):1879–1888, 2013.
- ²⁶Hirche, C., L. Xiong, C. Heffinger, M. Munzberg, S. Fischer, U. Kneser, and T. Kremer. Vascularized versus non-vascularized bone grafts in the treatment of scaphoid non-union. *J. Orthop. Surg. (Hong Kong)* 25(1):2309499016684291, 2017.
- ²⁷Hollister, S. J. Porous scaffold design for tissue engineering. *Nat. Mater.* 4(7):518–524, 2005.
- ²⁸Hui, P. W., P. C. Leung, and A. Sher. Fluid conductance of cancellous bone graft as a predictor for graft-host interface healing. *J. Biomech.* 29(1):123–132, 1996.
- ²⁹Kang, S.-W., J.-S. Kim, K.-S. Park, B.-H. Cha, J.-H. Shim, J. Y. Kim, D.-W. Cho, J.-W. Rhie, and S.-H. Lee. Surface modification with fibrin/hyaluronic acid hydrogel on solid-free form-based scaffolds followed by BMP-2 loading to enhance bone regeneration. *Bone* 48(2):298–306, 2011.
- ³⁰Kim, D., G. Pertea, C. Trapnell, H. Pimentel, R. Kelley, and S. L. Salzberg. TopHat2: accurate alignment of transcripts in the presence of insertions, deletions and gene fusions. *Genome Biol.* 14(4):R36, 2013.
- ³¹Knothe Tate, M. L. Interstitial fluid flow. In: *Bone Mechanics Handbook*, edited by S. C. Cowin. Boca Raton: CRC Press, 2001, pp. 221–229.
- ³²Kolar, P., K. Schmidt-Bleek, H. Schell, T. Gaber, D. Toben, G. Schmidmaier, C. Perka, F. Buttgerit, and G. N. Duda. The early fracture hematoma and its potential role in fracture healing. *Tissue Eng. B* 16(4):427–434, 2010.
- ³³Krishnan, L., C. J. Underwood, S. Maas, B. J. Ellis, T. C. Kode, J. B. Hoying, and J. A. Weiss. Effect of mechanical boundary conditions on orientation of angiogenic microvessels. *Cardiovasc. Res.* 78(2):324–332, 2008.
- ³⁴Krishnan, L., N. J. Willett, and R. E. Guldberg. Vascularization strategies for bone regeneration. *Ann. Biomed. Eng.* 42(2):432–444, 2014.
- ³⁵Laschke, M. W., Y. Harder, M. Amon, I. Martin, J. Farhadi, A. Ring, N. Torio-Padron, R. Schramm, M. Rücker, and D. Junker. Angiogenesis in tissue engineering: breathing life into constructed tissue substitutes. *Tissue Eng.* 12(8):2093–2104, 2006.
- ³⁶Laschke, M. W., S. Kleer, C. Scheuer, S. Schuler, P. Garcia, D. Eglin, M. Alini, and M. D. Menger. Vascularisation of porous scaffolds is improved by incorporation of adipose tissue-derived microvascular fragments. *Eur. Cell Mater.* 24:266–277, 2012.
- ³⁷Laschke, M. W., and M. D. Menger. Vascularization in tissue engineering: angiogenesis versus inosculation. *Eur. Surg. Res.* 48(2):85–92, 2012.
- ³⁸Laschke, M. W., and M. D. Menger. Adipose tissue-derived microvascular fragments: natural vascularization units for regenerative medicine. *Trends Biotechnol.* 33(8):442–448, 2015.
- ³⁹Lee, E., J.-Y. Ko, J. Kim, J.-W. Park, S. Lee, and G.-I. Im. Osteogenesis and angiogenesis are simultaneously enhanced in BMP2-/VEGF-transfected adipose stem cells

- through activation of the YAP/TAZ signaling pathway. *Biomater. Sci.* 7(11):4588–4602, 2019.
- ⁴⁰Lennon, D. P., and A. I. Caplan. Isolation of rat marrow-derived mesenchymal stem cells. *Exp. Hematol.* 34(11):1606–1607, 2006.
- ⁴¹Liao, Y., J. Wang, E. J. Jaehnig, Z. Shi, and B. Zhang. WebGestalt 2019: gene set analysis toolkit with revamped UIs and APIs. *Nucl. Acids Res.* 47(W1):W199–W205, 2019.
- ⁴²Liberzon, A., A. Subramanian, R. Pinchback, H. Thorvaldsdóttir, P. Tamayo, and J. P. Mesirov. Molecular signatures database (MSigDB) 3.0. *Bioinformatics* 27(12):1739–1740, 2011.
- ⁴³Love, M. I., W. Huber, and S. Anders. Moderated estimation of fold change and dispersion for RNA-seq data with DESeq2. *Genome Biol.* 15(12):550, 2014.
- ⁴⁴Maas, S. A., B. J. Ellis, G. A. Ateshian, and J. A. Weiss. FEBio: finite elements for biomechanics. *J. Biomech. Eng.* 134(1), 2012.
- ⁴⁵Maas, S. A., S. A. LaBelle, G. A. Ateshian, and J. A. Weiss. A plugin framework for extending the simulation capabilities of FEBio. *Biophys. J.* 115(9):1630–1637, 2018.
- ⁴⁶Malda, J., T. J. Klein, and Z. Upton. The roles of hypoxia in the in vitro engineering of tissues. *Tissue Eng.* 13(9):2153–2162, 2007.
- ⁴⁷Matsubara, H., D. E. Hogan, E. F. Morgan, D. P. Mortlock, T. A. Einhorn, and L. C. Gerstenfeld. Vascular tissues are a primary source of BMP2 expression during bone formation induced by distraction osteogenesis. *Bone* 51(1):168–180, 2012.
- ⁴⁸McDaniel, J. S., M. Pilia, C. L. Ward, B. E. Pollock, and C. R. Rathbone. Characterization and multilineage potential of cells derived from isolated microvascular fragments. *J. Surg. Res.* 192(1):214–222, 2014.
- ⁴⁹Müller, P., U. Bulnheim, A. Diener, F. Lüthen, M. Teller, E. D. Klinkenberg, H. G. Neumann, B. Nebe, A. Liebold, and G. Steinhoff. Calcium phosphate surfaces promote osteogenic differentiation of mesenchymal stem cells. *J. Cell Mol. Med.* 12(1):281–291, 2008.
- ⁵⁰Nagel, T., and D. J. Kelly. Apparent behaviour of charged and neutral materials with ellipsoidal fibre distributions and cross-validation of finite element implementations. *J. Mech. Behav. Biomed. Mater.* 9:122–129, 2012.
- ⁵¹Nauman, E. A., K. Fong, and T. Keaveny. Dependence of intertrabecular permeability on flow direction and anatomic site. *Ann. Biomed. Eng.* 27(4):517–524, 1999.
- ⁵²Nunes, S. S., L. Krishnan, C. S. Gerard, J. R. Dale, M. A. Maddie, R. L. Benton, and J. B. Hoying. Angiogenic potential of microvessel fragments is independent of the tissue of origin and can be influenced by the cellular composition of the implants. *Microcirculation* 17(7):557–567, 2010.
- ⁵³Park, K.-H., H. Kim, S. Moon, and K. Na. Bone morphogenic protein-2 (BMP-2) loaded nanoparticles mixed with human mesenchymal stem cell in fibrin hydrogel for bone tissue engineering. *J. Biosci. Bioeng.* 108(6):530–537, 2009.
- ⁵⁴Pilia, M., J. S. McDaniel, T. Guda, X. K. Chen, R. P. Rhoads, R. E. Allen, B. T. Corona, and C. R. Rathbone. Transplantation and perfusion of microvascular fragments in a rodent model of volumetric muscle loss injury. *Eur. Cell Mater.* 28:11–23, 2014; (discussion 23–4).
- ⁵⁵Pilia, M., J. McDaniel, T. Guda, X. Chen, R. Rhoads, R. E. Allen, B. Corona, and C. Rathbone. Transplantation and perfusion of microvascular fragments in a rodent model of volumetric muscle loss injury. *Eur. Cells Mater.* 28:11–24, 2014.
- ⁵⁶Pittenger, M. F., A. M. Mackay, S. C. Beck, R. K. Jaiswal, R. Douglas, J. D. Mosca, M. A. Moorman, D. W. Simonetti, S. Craig, and D. R. Marshak. Multilineage potential of adult human mesenchymal stem cells. *Science* 284(5411):143, 1999.
- ⁵⁷Pollock, B. E., C. R. Rathbone, J. C. Wenke, and T. Guda. Natural polymeric hydrogel evaluation for skeletal muscle tissue engineering. *J. Biomed. Mater. Res. B* 2017.
- ⁵⁸Rathbone, C., T. Guda, B. Singleton, D. Oh, M. Appleford, J. Ong, and J. Wenke. Effect of cell-seeded hydroxyapatite scaffolds on rabbit radius bone regeneration. *J. Biomed. Mater. Res. A* 102(5):1458–1466, 2014.
- ⁵⁹Ruehle, M. A., E. A. Eastburn, S. A. LaBelle, L. Krishnan, J. A. Weiss, J. D. Boerckel, L. B. Wood, R. E. Guldberg, and N. J. Willett. Mechanical regulation of microvascular angiogenesis. *bioRxiv* 2020.
- ⁶⁰Sander, E. A., and E. A. Nauman. Permeability of musculoskeletal tissues and scaffolding materials: experimental results and theoretical predictions. *Crit. Rev. Biomed. Eng.* 31(1–2):1–26, 2003.
- ⁶¹Santos, M. I., and R. L. Reis. Vascularization in bone tissue engineering: physiology, current strategies, major hurdles and future challenges. *Macromol. Biosci.* 10(1):12–27, 2010.
- ⁶²Santos, M. I., K. Tuzlakoglu, S. Fuchs, M. E. Gomes, K. Peters, R. E. Unger, E. Piskin, R. L. Reis, and C. J. Kirkpatrick. Endothelial cell colonization and angiogenic potential of combined nano- and micro-fibrous scaffolds for bone tissue engineering. *Biomaterials* 29(32):4306–4313, 2008.
- ⁶³Sato, N., Y. Sawasaki, A. Senoo, Y. Fuse, Y. Hirano, and T. Goto. Development of capillary networks from rat microvascular fragments in vitro: the role of myofibroblastic cells. *Microvasc. Res.* 33(2):194–210, 1987.
- ⁶⁴Schneider, C. A., W. S. Rasband, and K. W. Eliceiri. NIH Image to ImageJ: 25 years of image analysis. *Nat. Methods* 9(7):671, 2012.
- ⁶⁵Schumann, P., C. Von See, A. Kampmann, D. Lindhorst, F. Tavassol, H. Kokemüller, K. H. Bormann, N. C. Gellrich, and M. Rücker. Comparably accelerated vascularization by preincorporation of aortic fragments and mesenchymal stem cells in implanted tissue engineering constructs. *J. Biomed. Mater. Res. A* 97(4):383–394, 2011.
- ⁶⁶Später, T., F. Frueh, M. Menger, and M. Laschke. Potentials and limitations of Integra® flowable wound matrix seeded with adipose tissue-derived microvascular fragments. *Eur. Cells Mater. (ECM)* 33:268–278, 2017.
- ⁶⁷Stegen, S., S. Deprez, G. Eelen, S. Torrekens, R. Van Looveren, J. Goveia, B. Ghesquière, P. Carmeliet, and G. Carmeliet. Adequate hypoxia inducible factor 1 α signaling is indispensable for bone regeneration. *Bone* 87:176–186, 2016.
- ⁶⁸Stevens, M. M. Biomaterials for bone tissue engineering. *Mater. Today* 11(5):18–25, 2008.
- ⁶⁹Stiers, P.-J., N. van Gastel, and G. Carmeliet. Targeting the hypoxic response in bone tissue engineering: a balance between supply and consumption to improve bone regeneration. *Mol. Cell. Endocrinol.* 432:96–105, 2016.
- ⁷⁰Stone, I. R., and C. R. Rathbone. Microvascular fragment transplantation improves rat dorsal skin flap survival. *Plast. Reconstruct. Surg. Global Open* 4(12), 2016.
- ⁷¹Suva, L. J., G. J. Sedor, N. Endo, H. A. Quartuccio, D. D. Thompson, I. Bab, and G. A. Rodan. Pattern of gene

- expression following rat tibial marrow ablation. *J. Bone Miner. Res.* 8(3):379–388, 1993.
- ⁷²Tang, Y., and S. J. Weiss. Snail/Slug-YAP/TAZ complexes cooperatively regulate mesenchymal stem cell function and bone formation. *Cell Cycle* 16(5):399–405, 2017.
- ⁷³Team, R. C. R: a language and environment for statistical computing. New York: RC Team, 2013.
- ⁷⁴Tsigkou, O., I. Pomerantseva, J. A. Spencer, P. A. Redondo, A. R. Hart, E. O'Doherty, Y. Lin, C. C. Friedrich, L. Daheron, and C. P. Lin. Engineered vascularized bone grafts. *Proc. Natl. Acad. Sci.* 107(8):3311–3316, 2010.
- ⁷⁵Wang, X., A. F. Valls, G. Schermann, Y. Shen, I. M. Moya, L. Castro, S. Urban, G. M. Solecki, F. Winkler, L. Riedemann, R. K. Jain, M. Mazzone, T. Schmidt, T. Fischer, G. Halder, and C. R. de Almodovar. YAP/TAZ orchestrate VEGF signaling during developmental angiogenesis. *Dev. Cell* 42(5):462–478.e7, 2017.
- ⁷⁶Weinreb, M., D. Shinar, and G. A. Rodan. Different pattern of alkaline phosphatase, osteopontin, and osteocalcin expression in developing rat bone visualized by in situ hybridization. *J. Bone Miner. Res.* 5(8):831–842, 1990.
- ⁷⁷Yang, W., D. Guo, M. A. Harris, Y. Cui, J. Gluhak-Heinrich, J. Wu, X.-D. Chen, C. Skinner, J. S. Nyman, and J. R. Edwards. Bmp2 in osteoblasts of periosteum and trabecular bone links bone formation to vascularization and mesenchymal stem cells. *J. Cell Sci.* 126(18):4085–4098, 2013.
- ⁷⁸Yu, H., P. J. VandeVord, L. Mao, H. W. Matthew, P. H. Wooley, and S.-Y. Yang. Improved tissue-engineered bone regeneration by endothelial cell mediated vascularization. *Biomaterials* 30(4):508–517, 2009.
- ⁷⁹Yu, G., L. G. Wang, Y. Han, and Q. Y. He. clusterProfiler: an R package for comparing biological themes among gene clusters. *OMICS* 16(5):284–287, 2012.
- ⁸⁰Zhu, A., J. G. Ibrahim, and M. I. Love. Heavy-tailed prior distributions for sequence count data: removing the noise and preserving large differences. *Bioinformatics* 35(12):2084–2092, 2019.

Publisher's Note Springer Nature remains neutral with regard to jurisdictional claims in published maps and institutional affiliations.